Understanding star formation in NGC 4571 using UVIT and SDSS

A Thesis

submitted to

Indian Institute of Science Education and Research Pune

in partial fulfilment of the requirements for the

BS-MS Dual Degree Programme

by

Himanshu A Bhisikar

Indian Institute of Science Education and Research Pune

Dr. Homi Bhabha Road,

Pashan, Pune 411008, INDIA.

April, 2022

Supervisor: Dr. Kanak Saha

Certificate

This is to certify that this dissertation entitled ”Understanding star formation in NGC 4571 using UVIT and SDSS” towards the partial fulfilment of the BS-MS dual degree programme at the Indian Institute of Science Education and Research, Pune represents study/work carried out by **Himanshu A Bhisikar** at Indian Institute of Science Education and Research, Pune, under the supervision of **Dr. Kanak Saha**, Associate Professor, Department of Physics IUCAA-Pune, during the academic year 2021-2022.

Saha

Dr. Kanak Saha

Committee:

Dr. Kanak Saha

Dr. Ramana Athreya

Declaration

I hereby declare that the matter embodied in the report entitled ”Understanding star formation in NGC 4571 using UVIT and SDSS”, are the results of the work carried out by me at the Department of Physics, Indian Institute of Science Education and Research, Pune, under the supervision of **Dr. Kanak Saha**, and the same has not been submitted elsewhere for any other degree.

Himanshu

Himanshu A Bhisikar

Acknowledgements

This has been an unforgettable journey, and the learning experience has been exciting, humbling, and yet truly enlightening. There have been many ups and downs in this journey, but I have had the support from a lot of people who have constantly given me strength in the tough times whilst also encouraging me in the happiest of times.

I would like to express my deepest gratitude to my supervisor Dr. Kanak Saha, for his guidance and unwavering support throughout this project. He has been a constant source of motivation and his lessons have truly shaped the researcher in me.

I would like to thank my TAC member, Dr. Ramana Athreya, as he was the one who introduced me to the hard graft that is research. Under his guidance, I learnt how to think independently and to be a better student.

I would like to thank Dr. Chayan Mondal (Post Doctoral Fellow at IUCAA), who has been my mentor in IUCAA ever since the project started. It was under him that I truly grasped the concepts and learnings of the project. I would also like to thank Anshuman Borgohain (PhD Student at Tezpur University) for getting me up to speed with the project in the initial phases.

I would like to thank my family and my extended family for their constant prayers, unconditional support, and the best of wishes. I would also like to thank all my friends for always being on my side and for all their help and encouragement.

Finally, I would like to thank IISER, Pune for allowing us students to pursue our MS projects at an institute of our choice. This was truly a rewarding opportunity, and I am deeply grateful to have been able to explore a new institute and an interesting field of study.

Abstract

Star formation is one of the key processes through which galaxies convert their gas into stars, and that in turn leads to the stellar mass growth of a galaxy. Not only that, star formation is the key parameter that divides the galaxy into two primary categories: star-forming galaxies and quenched galaxies. A comprehensive multi-wavelength study is necessary in order to gain critical insights on the physical properties of a galaxy. This thesis investigates the nature of star formation in the flocculent galaxy NGC 4571 using multi-band observations taken from the Ultra-Violet Imaging Telescope (UVIT) in 2 filters - F154W and N263M and the Sloan Digital Sky Survey (SDSS) in 5 filters - u, g, r, i, z. We perform image analysis using a variety of tools such as SExtractor, ds9, topcat. We also use various python libraries such as astropy and photutils for photometry. With the superior spatial resolution of UVIT ($\sim 1.4''$), we identified 172 bright young star-forming regions in the UVIT bands within the galaxy, most of them having sizes between $\sim 100-400$ pc. These regions were also found to be clumpy in nature. Around 53% of the sources are younger than ~ 20 Myr, which points towards a recent spike in star formation. We also noticed that the younger sources are distributed throughout the galaxy, which is an indicator of recent star formation across the galaxy. We also found that most of the sources are roughly circular, with ellipticity $\varepsilon < 0.5$ and that there is no specific trend observed with regards to the orientation of the major axis of the identified sources. We further derived the radial surface brightness profile in UV and optical, the radial FUV-NUV color profile, and the radial SFR density profile of the galaxy, which provide further evidence for star formation occurring throughout the galaxy. Based on the UVIT data, the star formation rate in NGC 4571 is found to be $\sim 0.01605\ M_{\odot}/yr$.

Contents

List of Figures

List of Tables

Chapter 1

Introduction

1.1 Galaxies and their evolution

When Edwin Hubble pointed the 100-inch Hooker telescope to the sky about a hundred years ago, he discovered that the galaxies he saw could be broadly divided into two distinct classes according to morphology: spiral and elliptical. It is now well-accepted that the structural and kinematic properties of a galaxy is determined predominantly by the presence, acquisition, and distribution of angular momentum [19]. Whilst elliptical galaxies are formed by losing angular momentum, the spiral galaxies form by preserving and re-distributing the angular momentum. The formation process is therefore dramatically different for both the types of galaxies as an elliptical galaxy is formed by efficient cooling of infalling gas, this consequently makes the galaxy redder and it is also quenched upon its formation due to the consumption of cold gas, whereas a spiral galaxy is formed in the host dark matter halo with fixed fractions of the mass and angular momentum of the halo, and once formed, the disk gradually grows through continuous in-situ star formation, along with long-standing gas accretion processes [8]. Large multi-band photometric surveys have established that the morphology of galaxies is closely related to their colors, in the sense that the spiral galaxies are usually blue and the elliptical galaxies are predominantly red [17]. As blue colors are indicative of ongoing/recent star formation, this relation indicates that the quenching of star formation in galaxies may be accompanied by structural transformation.

Star formation is one of the most important processes which govern the formation and evolution of galaxies [22]. The distribution of star-forming regions in the disks of galaxies, and their association with spiral arms and bars can reveal the possible mechanisms in which star formation is triggered in galaxies [20]. It can also shed light on the evolution of star clusters over time [7]. The distribution of star-forming regions over the spiral arms of the galaxy is an important way to probe the spiral structure. [21].

The star formation in galaxies is measured primarily by using the star formation Rate (SFR), which is in terms of the mass of stars formed per unit year. [33] and [24] derived the first expressions for SFR from the evolutionary synthesis models of galaxies. With recent advancements in techniques and the development of more direct and precise SFR diagnostics, we now have a variety of star formation tracers that cover a wide range of wavelengths which can be used to estimate the SFR of galaxies. Two of the best tracers of star formation are the H_α and the Far Ultraviolet (FUV) luminosity of galaxies. Whilst H_α measures the star formation which is only a few million years old, the FUV emission traces the stars that have ages from a few million years to $\sim 10^8$ yrs [16]

The Ultra-violet (UV) flux is one of the best tracers of star formation in galaxies [27]. The Far-UV (FUV) region is an ideal window to detect and study the massive, hot young stars like the O, B type stars, Blue Horizontal Branch (BHB) stars and White dwarfs (WDs) [13]. They are the principal locations for the synthesis of heavy elements [2]. The Near-UV (NUV) emission, however, traces the less massive stars such as the A-type stars, which are more common. NUV emission therefore has a larger spatial extent as when compared to FUV [14]. The spatial distribution of FUV and NUV emission is, therefore, a good indicator of the recent star formation in galaxy disks and its effect on galaxy evolution [11]

1.2 Galaxy cluster

A galaxy cluster is defined as a large-scale structure containing hundreds to thousands of galaxies. They are some of the largest gravitationally-bound structures in the Universe, and as such are powerful tools for a variety of research areas in both astrophysics and cosmology. Due to their high density, clusters of galaxies are good laboratories to study the effect of the environment on individual galaxies and their evolution [15], whilst also being used to study their effects on the surrounding Inter-Galactic Medium (IGM). Such clusters are also frequently used as gravitational lenses to observe galaxies that are faint or have a high redshift value [12]

1.3 Virgo cluster

The Virgo Cluster is the closest and best-studied cluster of galaxies. Lying at a distance of approximately 20 Mpc in the constellation of Virgo, it has ~ 1300 galaxies of various morphologies in it. There have been several studies indicative of the fact that galaxies in the core of the Virgo cluster have certain peculiar properties when compared to galaxies of similar morphological types, the most common of which are low H(I) contents and low star formation rates [10], [26]. The most commonly accepted interpretation for this is the mechanism of Ram Pressure Stripping, which occours when galaxies are moving through the dense IGM in the cluster. [26] had identified a few galaxies with extreme properties wherein the galaxies were of the morphological type Sc, but their color, H(I) content, and star formation rates were similar to Sb galaxies.

1.4 NGC 4571

NGC 4571 (UGC 7788) is a late-type spiral galaxy belonging to the Virgo cluster, and located in the constellation of Coma Berenices. UV and optical images clearly show that it is a face-on galaxy with a multi-armed spiral structure. The morphological type of the galaxy is SA(r)d. NGC 4571 is an anemic galaxy [34]. Galaxies of this type possess characteristics that are intermediate between those of S0 galaxies and normal spiral galaxies, and are characterized by a lack of gas and a low rate of star formation. We list some of the properties of the galaxy in table 1.1.

Table 1.1: Properties of NGC 4571

Property	Value	Units	Reference
RA	12h 36m 56.38s	J2000d	Janice C. Lee et al.(2021)
DEC	+14d 13m 02.05s	J2000d	Janice C. Lee et al.(2021)
Type	SA(r)d		de Vaucouleurs et al.(1991)
Distance	14.9 ± 1.2	Mpc	Janice C. Lee et al.(2021)
Position Angle (PA)	$40^o \pm 2^o$	Degrees	van der Hulst et al.(1987)
Inclination (i)	$34^o \pm 4^o$	Degrees	van der Hulst et al.(1987)
Diameter (D_{25})	22.1	Kpc	Young et al.(1996)
Stellar Mass	3.2×10^{10}	$M_\odot$	Leroy et al. (2019)

The classification of the galaxy is supported by its luminosity profile, which is seen to be dominated by the disk. It has a small bulge component which contributes $\approx 4\%$ to the integrated luminosity of the galaxy. In most of the other respects, NGC 4571 is unlike any galaxy belonging to its morphological classification as pointed out by [26]. The current star formation rate of the galaxy is relatively low, and the total H_α luminosity and the characteristic luminosities of the brightest H(II) regions are lower by more than a factor of 3 when compared to the normal value for a typical Sc galaxy. The broadband colors which were determined from BVR photometry carried out are unusually red (B-V = 0.70), which is consistent with the low star formation rate. This also suggests that the stellar disk has evolved and probably has not been subjected to active star formation in recent years.

NGC 4571 was studied in detail using the NRAO VLA in the 1 km configuration to study the H(I) regions. The neutral Hydrogen (H(I)) gas properties of NGC 4571 are quite unusual. There is an H(I) deficiency visible in the inner parts, which is usually more typical for the Sa and Sb types of galaxies [3]. Another peculiar fact is that the column densities of H(I) are low across the disk. The peak values reach up to 4×10^{20} $atoms/cm^2$, which is a factor of 5 below the normal values for Sc galaxies. The total amount of neutral gas present is 1.5×10^9 $M_\odot$ for an assumed distance of 21.9 Mpc. The ratio of the H(I) mass to total mass is found to be 0.03. Another very striking property of the H(I) disk is its small size as compared to the optical diameter. These measurements of the H(I) surface density are quite reliable. with a value of 0.89 for the ratio of H(I) to optical diameter. The H(I) size at 1.93×10^{20} $atoms/cm^2$ [3] is roughly $3.2'$, while the De Vaucouleurs diameter measures $3.7'$. This is a very unusual property for galaxies in the field, but is not uncommon for galaxies located in the central region of the Virgo cluster This property is something which is expected from simple models of Ram pressure stripping. It is also clear that neither of the stellar and H(I) disk extends much beyond 10 kpc.

The low H(I) content and small H(I) diameter, along with the optical properties are consistent with a slow gas removal process, perhaps by the process of Ram-pressure sweeping. The overall low gas density is also consistent with the low star formation rate and red disk colors. It also confirms the findings of [10] that anemic galaxies in the Virgo cluster have low gas surface densities. This relation between anemia and the gas surface density however, is not always seen in the clusters which are more distant [26].

The galaxy has also been studied by the Mt. Lemmon, Mt. Palomar and Kitt Peak National Observatory facilities. These were used to obtain optical continuum, and He data. The galaxy has also been imaged by the Sloan Digital Sky Survey (SDSS) [9] in 5 filters - u, g, r, i, z, and by the UV survey mission GALEX [30] in the FUV and NUV wavebands, indicating ongoing star-formation.

For our study, we used the Ultra Violet Imaging Telescope (UVIT) and carried out observations of the galaxy in 2 filters, the FUV F154W filter and the NUV N263M filter. Our primary aim was to explore the star-forming regions and to study the nature of star-formation occurring in this galaxy. With the large field of view of UVIT, we were able to image the galaxy well beyond its optical radius. This gave us the opportunity to study and understand the overall disk structure in UV and to also pick up the young star-forming clumps across the disk including in the outskirts of the galaxy. UVIT also has a smaller value of angular resolution $\sim 1.4''$, as compared with the previous dedicated UV survey mission GALEX, which had an angular resolution of $4.3'' - 5.3''$. This made UVIT an ideal instrument to study star-forming regions up to smaller scales, especially in the nearby face-on galaxies, wherein it can resolve large star clusters associated with the spiral arms of the galaxy.

NGC 4571 is a bright galaxy, with the SDSS optical images (g and r) and the UVIT images (FUV and NUV) showing prominent star-forming regions associated with the spiral arms of the galaxy. The arms are not well-defined in the optical images, but the morphology of the galaxy as seen from the UVIT observations indicated the structure to be a flocculent spiral. These star-forming regions are made of young stars, gas, and dust. There are multiple arms visible in the UVIT and SDSS optical images, but the number and structure of these arms is not clear in any of the images. The UVIT images show a small nucleus in the center of the galaxy, this being in contrast with the SDSS optical images wherein we see a significant bulge in the galaxy center.

Though the galaxy has been imaged and studied in various bands including UV, a detailed study combining FUV and NUV data together has not been done yet. This study provides a comprehensive view of the young star-forming regions in the galaxy. The deep and high-resolution UV images are utilised to identify star-forming clumps and estimate their age using simple stellar population (SSP) models. The study also derives the spatial distribution of young stellar clumps as a function of their age across the entire disk.

Chapter 2

Data and Observations

2.1 AstroSat

AstroSat is India's first Multi-wavelength space observatory, launched by the Indian Space Research Organization (ISRO) in 2015. The objectives of AstroSat are to study celestial sources in the X-ray, Optical and UV spectral bands simultaneously. The payloads present in AstroSat cover the energy bands of Ultraviolet (Near and Far), the Optical band and X-ray regime (0.3 keV to 100 keV). A unique capability of AstroSat is its ability to carry out simultaneous multi-wavelength observations of astronomical objects.

Figure 2.1: Payloads on board AstroSat ©http://astrosat.iucaa.in/

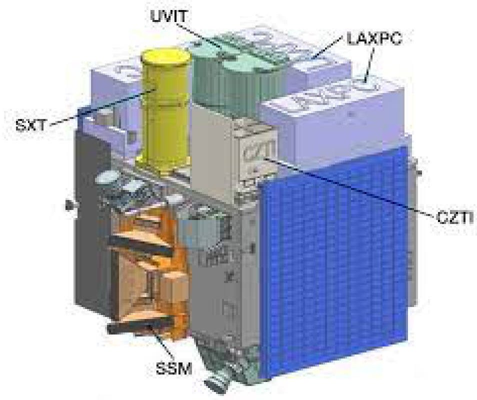

The payloads on board AstroSat are listed below -

- UVIT - Ultra-Violet Imaging Telescope
- LAXPC - Large-Area X-ray Proportional Counters
- CZTI - Cadmium-Zinc-Telluride Imager
- SXT - Soft X-ray imaging Telescope
- SSM - Scanning Sky Monitor

2.2 Ultra-Violet Imaging Telescope (UVIT)

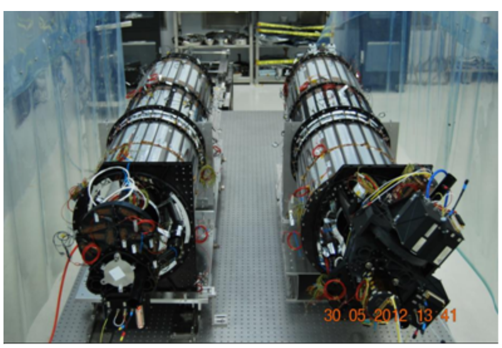

Figure 2.2: UVIT before being integrated in AstroSat ©https://www.isro.gov.in/astrosat/ultra-violet-imaging-telescope-uvit

One of the payloads present in AstroSat is the Ultra Violet Imaging Telescope (UVIT) [28], which is primarily an imaging instrument. This instrument comprises of two telescopes and can carry out observations simultaneously in three channels: FUV (130-180 nm), NUV (200-300 nm), and VIS (320-550 nm). Each one of these channels consist of a multiple number of filters, each with a different and unique bandwidth. The in-orbit calibration of the instrument was completed using HZ4 as the calibration source [23]. The magnitude system adopted for the filters in UVIT is the AB system. UVIT has a spatial resolution of $\sim 1.4''$ and a field of view diameter of ~ 0.5 degree. These numbers compare well with the GALEX telescope launched by NASA, which had a larger field of view diameter of ~ 1.2 degree, but a larger value of spatial resolution of $\sim 5.0''$.

The UVIT telescopes offer a unique set of capabilities, with some of its primary strengths being arc-second resolution over a wide field of view, time resolution as short as 600 Hz, a wide range of filters and gratings in FUV and NUV, simultaneous observations in the FUV, NUV and Visible bands, and simultaneous observations alongside X-ray timing and imaging telescopes onboard AstroSat. AstroSat has an orbit period of about 90 min, and the observations are mostly carried out in the night part of the orbit. The instrument then takes observations over several orbits so as to complete the required exposure time.

The UVIT has a very wide range of scientific objectives, extending from solar system objects to galaxy clusters. Some of the major scientific topics that are important to UVIT mission are Multi-wavelength study of X-ray sources, Hot Stars and White Dwarfs, Cataclysmic Variables and X-ray binaries, High mass stars and Luminous blue variables, Dust Extinction Studies, Quasars and Active Galactic Nuclei, UV morphology of Galaxies, and Deep Surveys

2.3 UVIT Data

The galaxy NGC 4571 was imaged in UV with the Ultra Violet Imaging Telescope (UVIT) onboard the AstroSat satellite. The images were processed from a targeted proposal with PI - Dr. Kanak Saha, Proposal ID - G06_016, Observation ID - G06_016T01_9000001052, Observation Date - 25-Feb-2017. The observations for the galaxy were taken in two filters, one in the FUV band (F154W : 1340-1800 Å) and one in the NUV band (N263M : 2461-2845 Å). 1 pixel of the FUV and NUV images corresponds to $\sim 0.4173''$ (≈ 28.7 *pc* at the distance of NGC 4571). The images were processed using a software named UVIT Pipeline. The pipeline corrects for any geometric distortion, flat field illumination, and spacecraft drift present. The images are then aligned and combined to create a science ready image. The details of UVIT observations of NGC 4571 are given in table 2.1.

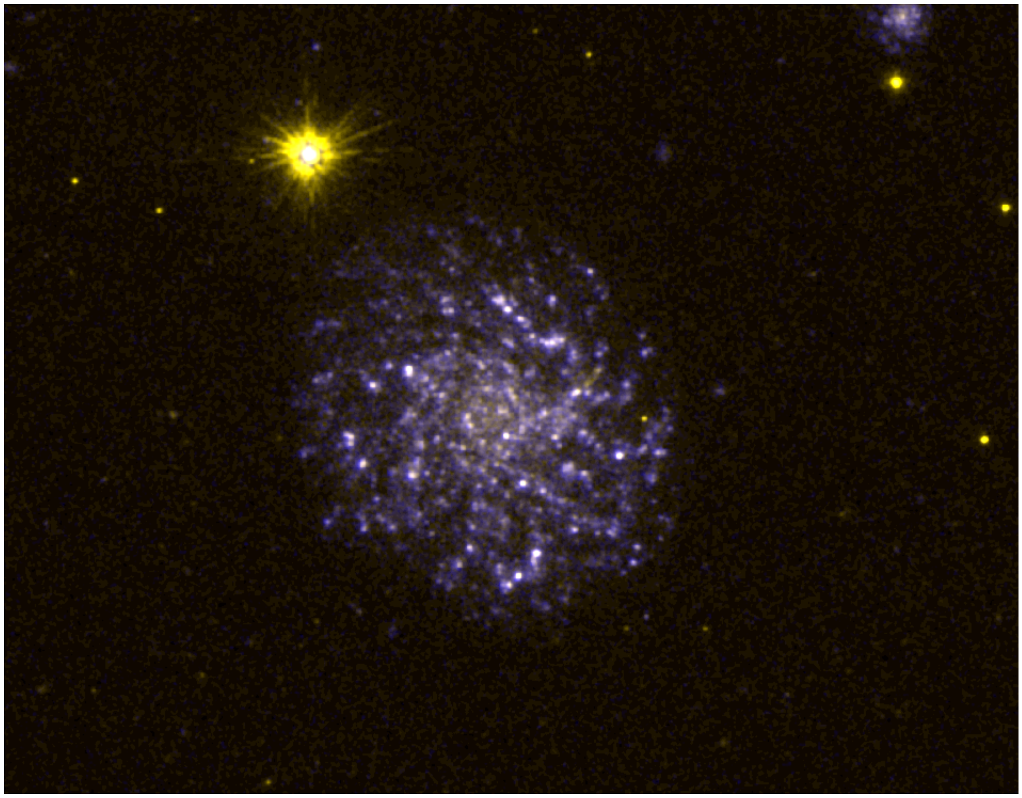

Figure 2.3: UVIT color composite image of the galaxy NGC 4571. The emissions in F154W and N263M filters are represented by blue and yellow color respectively.

Table 2.1: Details of UVIT Observations

Filter	Bandpass (Å)	ZP Magnitude (AB)	Unit conversion ($erg\ sec^{-1}\ cm^{-2}\ \AA^{-1}$)	$\Delta\lambda$ (Å)	Exposure time (sec)
F154W	1340 - 1800	17.765	3.593×10^{-15}	380	9853
N263M	2461 - 2845	18.180	8.440×10^{-16}	275	9650

The difference in angular resolution between UVIT and GALEX is best visible in the comparison of images taken by them, as seen in Figure 2.4 and 2.5. We can clearly see the clumps being resolved to a much greater degree in UVIT than when compared with GALEX. This difference is visible in both FUV as well as NUV image.

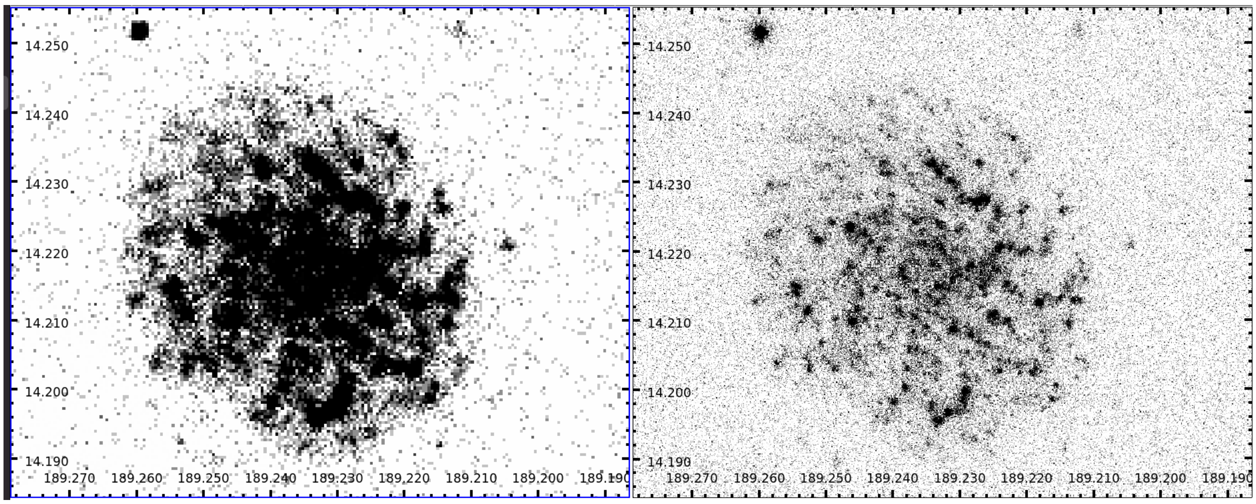

Figure 2.4: GALEX-FUV (left) and UVIT-FUV (right) images of NGC 4571

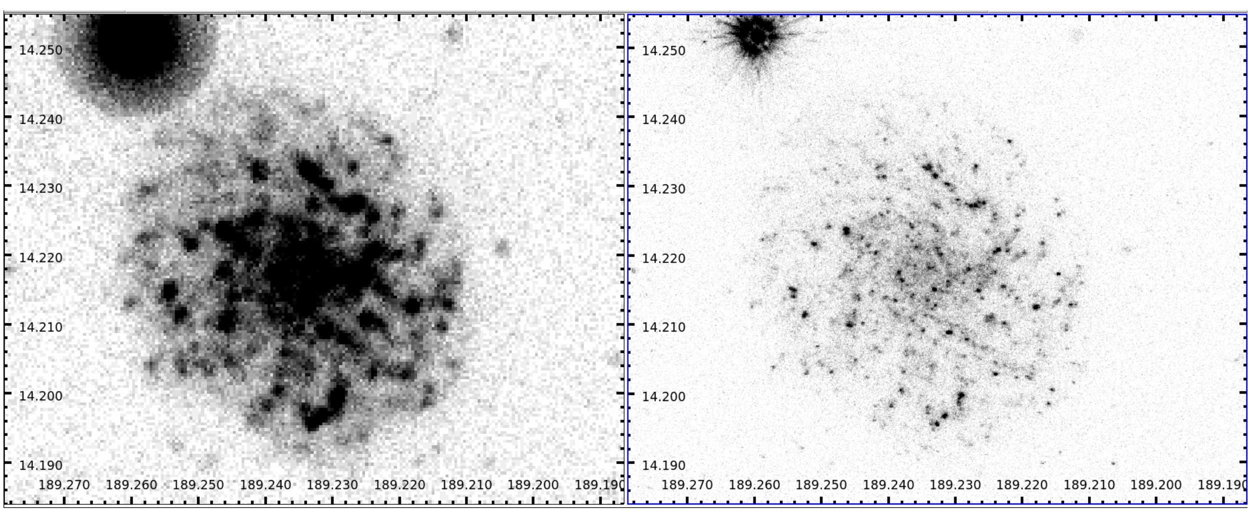

Figure 2.5: GALEX-NUV (left) and UVIT-NUV (right) images of NGC 4571

2.4 SDSS Data

The SDSS images of NGC 4571 were obtained from the SDSS Data Release 12 (DR12) Science Archive Server (SAS). The observations for the galaxy were taken in five filters - u $(3250-3800Å)$ g $(4085-5455Å)$, r $(5550-6915Å)$, i $(6850-8400Å)$, and z $(8650-9600Å)$. 1 pixel of the SDSS images correspond to $\sim 0.3961''$. The details of SDSS observations of NGC 4571 are given in Table 2.2.

Shown in Figure 2.6 are the effective area curves for the UVIT and the SDSS filters used in our analysis. The UVIT and SDSS data were obtained from [23] and [18] respectively.

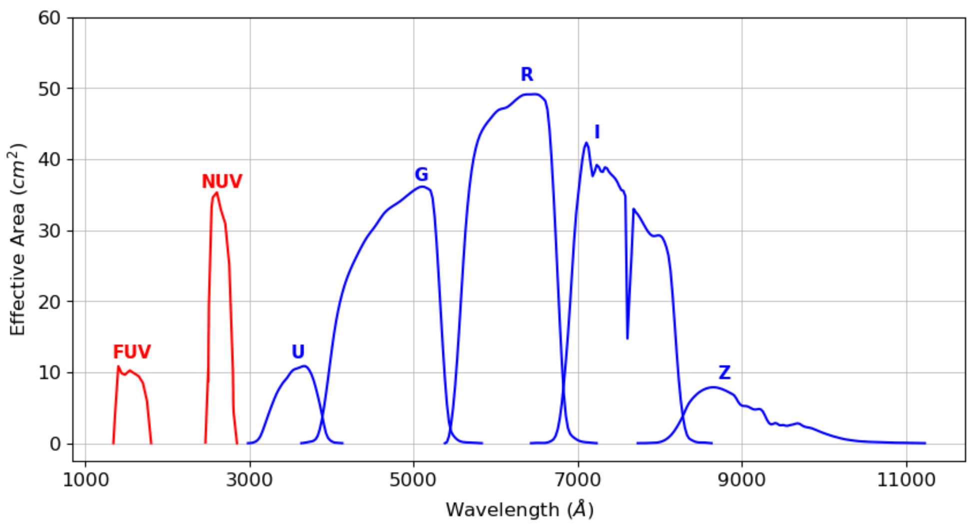

Figure 2.6: The Effective area curves of UVIT and SDSS filters

Figure 2.7: SDSS color composite image of the galaxy NGC 4571 (©2006 Michael R. Blanton & David W. Hogg)

Table 2.2: Details of SDSS Observations

Filter	Bandpass (Å)	ZP Magnitude (AB)	Unit conversion ($erg\ sec^{-1}\ cm^{-2}\ \AA^{-1}$)	$\Delta\lambda$ (Å)	Exposure time (sec)
u	3250-3800	24.63	8.67×10^{-18}	550	53.9
g	4085-5455	25.11	4.78×10^{-18}	1370	53.9
r	5550-6915	24.80	2.80×10^{-18}	1365	53.9
i	6850-8400	24.36	1.87×10^{-18}	1550	53.9
z	8650-9600	22.83	1.30×10^{-18}	950	53.9

Chapter 3

Methodology

3.1 Background Estimation

We estimated and accounted for the background value of flux in the images, which in turn determines the Signal-to-Noise ratio of the objects. A higher value of SNR indicates that the background flux value of the image is relatively low, and that it is easier to resolve between the background and prospective sources. We performed photometry on the sources that we detect, and it could be the case that the source flux might have a contribution from the background flux. It is thus important to account for and subtract the background flux value from the source flux value, as the flux value of the source should only contain the contribution from the source, and not from anywhere else.

To estimate background flux value, we first create the segmentation check-image using the publicly available software SEXtractor [1] software. The configuration parameters in the input file CHECKIMAGE_TYPE allows us to provide a list of check-image types to be produced by SExtractor. The segmentation check-image displays patches corresponding to pixels attributed to each detected object. It also shows whether the objects are broken up too much or not. We load the Segmentation image, create 75 apertures each of size 10×10 pixels, and place these apertures in random locations all around the image. We then performed aperture photometry on these apertures and extracted the flux values in each of the apertures. We then filter and exclude those apertures which lie on the segmented pixels and have a non-zero flux value. We overlay the remaining selected apertures on the main FITS image to perform a sanity check on the locations of the apertures and whether they lie on a source or not. We now add the original image and the segmented image and perform aperture photometry of the selected apertures on this resultant image. The flux values extracted from this instance of aperture photometry would give us the value of the background flux. We then divide the flux value by the area of each box to get the background flux value per *pixel* and plot a histogram to look at the trend of the background flux values. We fit a gaussian curve to the histogram and extract the mean and variance of the distribution, and repeat this procedure for all the 7 images to estimate the background flux in each image. We make sure to subtract this value from any photometric analysis that will be done during the course of our work.

3.2 Identification of star-forming clumps

The presence of FUV bright regions is an indicator of the presence of young star-forming regions in galaxies. These regions are often rich in gas and dust. The identification of FUV and NUV sources from their corresponding images was carried out using SExtractor. SExtractor is ideal for our usage as it uses the method of thresholding to locate the clumps - It divides the clumps into 32 equally-spaced levels between the peak value of the source and the detection threshold defined. The software then looks for the presence of another peak with its intensity exceeding a defined fraction of total intensity. If it is indeed the case, a new source is extracted. We set the value for DETECT_MINAREA to be 10 and the DETECT_THRESH values to be 2.25 for UVIT and 1.50 for SDSS respectively. The reason for the choice of DETECT_MINAREA is to enable the size of the smallest clump which can be detected to be similar in size to the width of the PSF of the image in consideration. As far as the choice for an appropriate value of DETECT_THRESH is concerned, the key point is to select a value which ensures that no pixels from the background are categorized as sources, which requires for us to have an accurate estimate of the background value of the image. Other input parameters are determined from tests carried out on the images, designed to optimize the detection of sources in the images.

A caveat of the thresholding process is that increasing the deblending will lead to single sources being classified as multiple sources, therefore resulting in an increase in the total number of sources. It is therefore necessary to optimize the deblending parameters to ensure the right number of sources are being identified.

For each image, we run the SEXtractor code and generate an output file containing various output parameters, some of them being the RA (Right ascension), DEC (Declination), A_IMAGE (Length of semi-major axis of AUTO aperture), B_IMAGE (Length of semi-minor axis of AUTO aperture), THETA_IMAGE (Position angle of A axis relative to the image axis), ELLIPTICITY (1-B/A of the identified source), and KRON_RADIUS (radius enclosing 90% of an object's flux). We then overlay the positions of the detected sources on the image itself and verify our output with the help of ds9 [31], which is an image display and visualization tool for astronomical data.

The image information, parameter information and observations are summarized in table 3.1 -

S No.	Filter	1 pixel = *arcsec*	PSF FWHM ($arcsec$)	DETECT_THRESH	Sources detected
1.	F154W	0.4171	1.40	2.25	416
2.	N263M	0.4173	1.40	2.25	461
3.	u	0.3961	2.31	1.50	60
4.	g	0.3960	1.48	1.50	361
5.	r	0.3960	1.48	1.50	383
6.	i	0.3960	1.73	1.50	265
7.	z	0.3961	1.70	1.50	108

Table 3.1: Properties of Pixel, FWHM, and detected sources of the images

Attached are the images of the observations at defined DETECT_THRESH. These images contain two images within them, the image and the image with the source catalog plotted on top of it. This will help us to compare and look at the identified sources as the images are side-by-side.

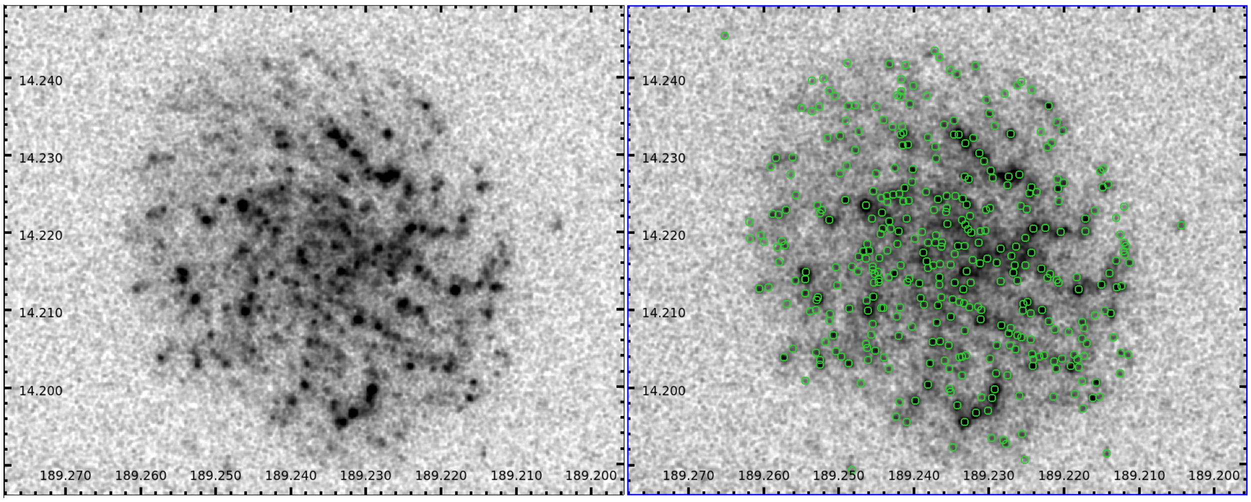

Figure 3.1: FUV-filter image and FUV-filter detected sources overlayed

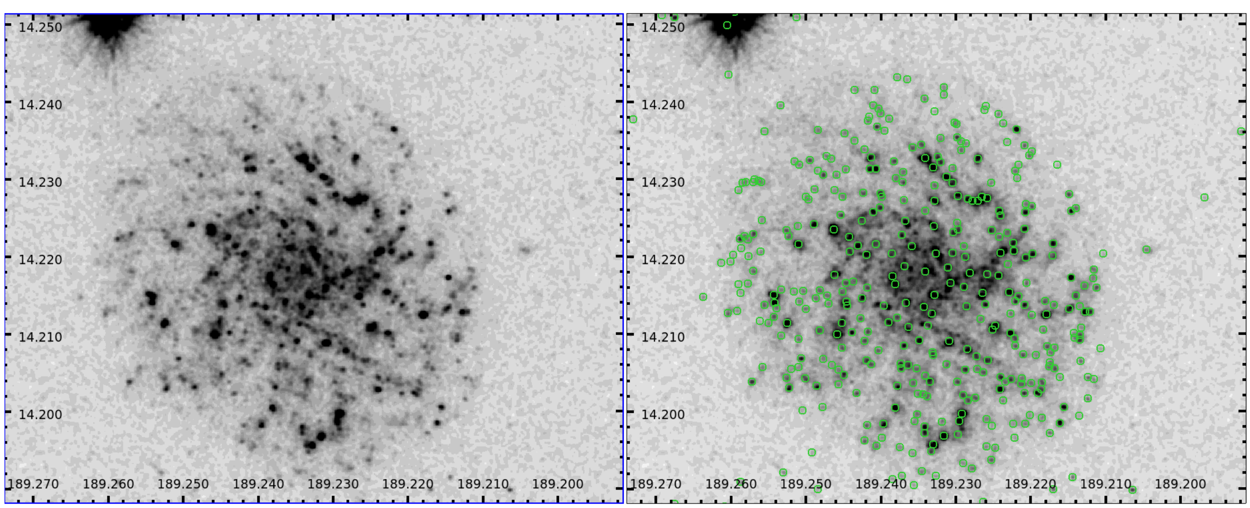

Figure 3.2: NUV-filter image and NUV-filter detected sources overlayed

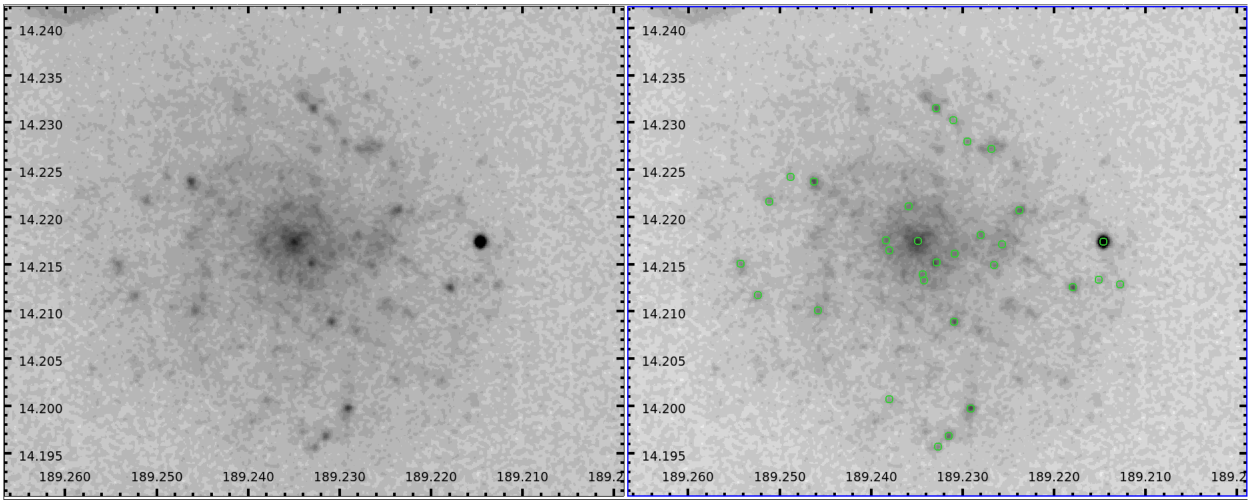

Figure 3.3: u-filter image and u-filter detected sources overlayed

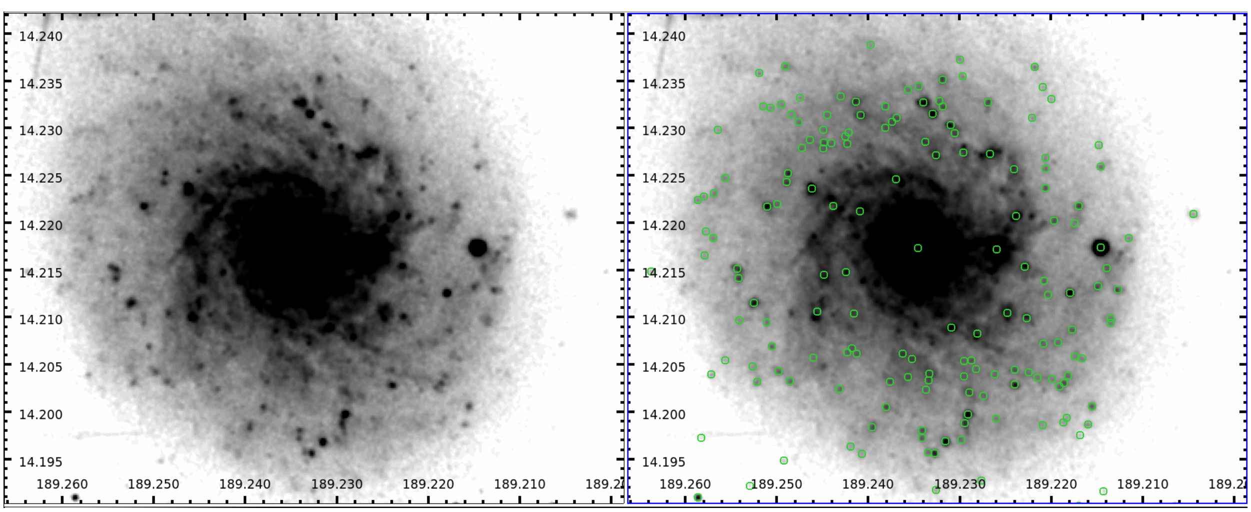

Figure 3.4: g-filter image and g-filter detected sources overlayed

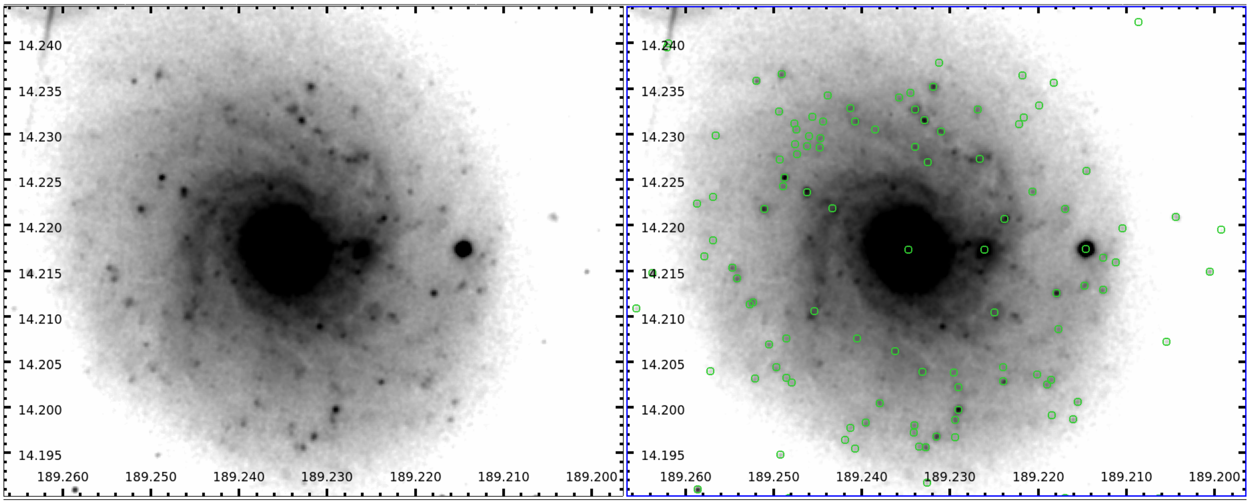

Figure 3.5: r-filter image and r-filter detected sources overlayed

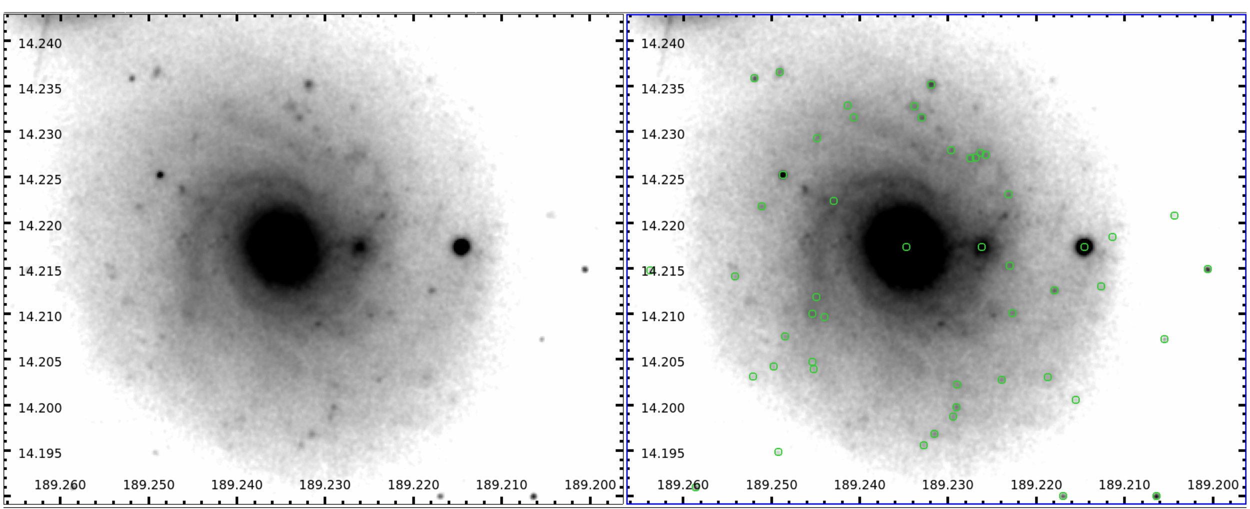

Figure 3.6: i-filter image and i-filter detected sources overlayed

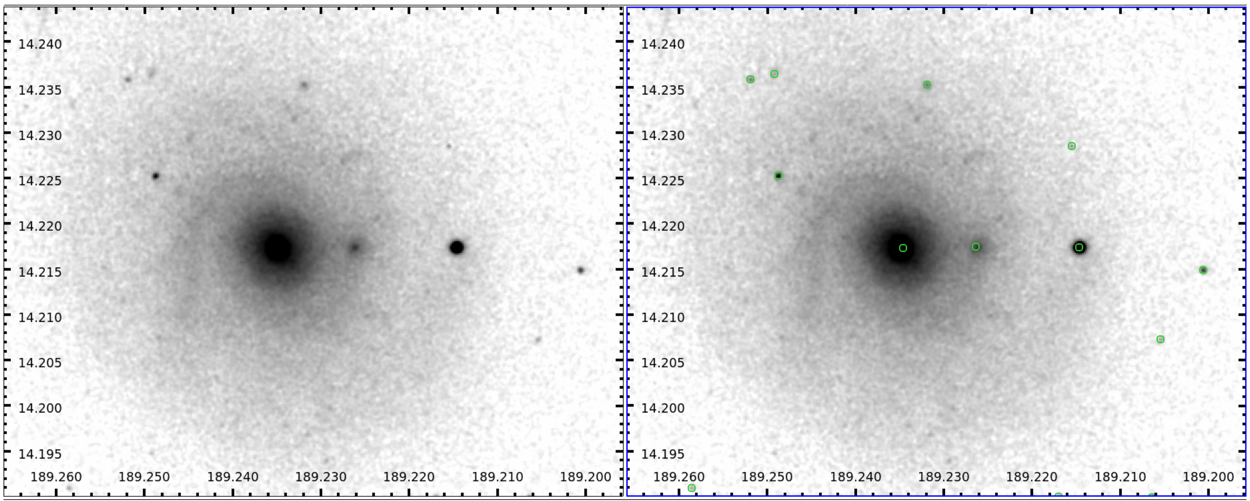

Figure 3.7: z-filter image and z-filter detected sources overlayed

After performing source extraction on the images, we now have the number of sources from each image. FUV and NUV have the most number of sources identified in the galaxy, followed by the g and r filters, and the i, u, and z filters end the list. As far as the UVIT FUV and NUV images are concerned, we can clearly see that the sources detected are from all around the galaxy, and that no local regions are preferred. The flocculent structure of the arms of the galaxy is also visible. The SDSS images show a different set of characteristics due to the images being taken in different wavelengths. The g and r filters have the most sources detected, and they are localized in a ringed shape all around the galaxy. The number of identified sources in the u, i, and z filters is much lower when compared with the g or r filters. The optical SDSS images are different from the UVIT images in that the central region of the galaxy is very crowded in the optical band, therefore making it hard to detect clumps there, and the outer parts of the galaxy shows low emission in the optical bands.

3.3 Catalog matching

We then carried out catalog matching, which is the procedure of finding out the common sources identified in the images in consideration. Since the presence of FUV and NUV bright regions is a good indicator of star formation occurring in the galaxy, we extracted the common sources from these 2 images and construct a common catalog of sources, which would then be used as our reference. We first extracted the sources from the individual image as detailed in section 3.1. We then used a software named topcat [32] to find the common sources. topcat is an interactive graphical viewer and editor for tabular data. It provides facilities that helps in analysis and manipulation of source catalogs and other kinds of tables. We loaded the tables into the software and specified the maximum radius of cross-matching to be 1 arcsec. This value is chosen as we have a crowded field, and it can be the case that we have multiple sources located close to each other. Choosing a smaller value reduces the probability of selecting the wrong source. Here, we specified the FUV table as the base table to which common sources from the NUV table are cross-matched and tabulated.

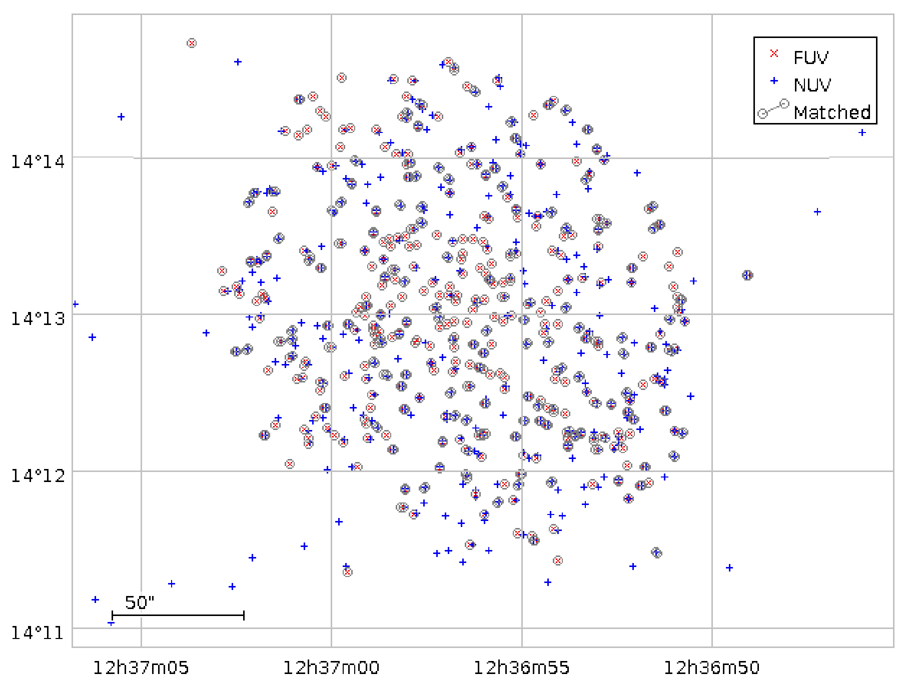

Figure 3.8: Catalog Matching between the FUV and NUV sources

3.4 Excluding Foreground stars and other sources

We then excluded stars and other objects which are not a part of the galaxy. This is a crucial step as there could be objects in our image which aren't a part of the analysis. Examples of such sources include foreground stars and galaxies found in the background. For our analysis, we use the Gaia and 2MASS catalogs to search for objects. Gaia gave us 53 objects whereas 2MASS gave us 117. We added both the catalogs, removed the common sources in both the catalogs, and created an overall list of sources. We then carried out cross-matching with the catalog created in 3.2, and remove objects common to both the catalogs.

3.5 Aperture Photometry

After obtaining the final catalog of sources and estimating the background value of the images, we carried out aperture photometry on all the detected sources. We carried out the process for the sources detected in both FUV and NUV, the only point being that instead of doing it only on the FUV and NUV image, we did it for all the 7 images (2 UVIT + 5 SDSS). This procedure is done regardless of the presence or absence of the source in the SDSS images, for reasons mentioned in Section 3.7.

We extracted the properties of the detected sources from the SEXtractor output file - RA (Right ascension), DEC (Declination), A_IMAGE (Length of semi-major axis), B_IMAGE (Length of semi-minor axis), THETA_IMAGE (Position angle of major axis). We then created custom elliptical apertures for all the detected sources, and used the aperture_photometry tool from the python package *photutils* to perform photometry on the above-defined apertures. We then obtained the flux values of each source and calculated the magnitude values of all sources in the corresponding bands.

3.6 Extinction Correction

One of the important factors that need to be considered while studying an external galaxy in UV is the effect of extinction. This is in part due to the higher-than-usual value of the extinction coefficients in UV wavelengths, and also due to the characteristic variation of extinction law in different galaxies. In order to estimate the extinction value in UVIT filters, we adopted the value of $E(B-V)$ = 0.047 (NED Database) for NGC 4571. The equation relating R_λ - the ratio of Total to selective absorption at λ, $E(B-V)$ - the excess reddening, and A_λ - the Total absorption (in mags) at λ is -

$$A_\lambda = R_\lambda \cdot E(B-V)$$

We used the Interstellar extinction law calculator of Doug Welch [4] available in the NASA / IPAC Extra-galactic Database (NED) to estimate the values of the extinction coefficients R_λ in the F154W and N263M bands and the SDSS bands too. We take the R_V values to be equal to 3.1, which is the value corresponding to the Milky way. Using the value of R_λ and $E(B-V)$ in the above equation, we estimated the value of extinctions in both the bands. The values of A_{F154W}, A_{N263M}, A_u, A_g, A_r, A_i, A_z are found to be 0.3811, 0.3081, 0.2319, 0.1678, 0.1250, 0.0913 and 0.0662 mag respectively. We used these values to correct the observed flux of the identified objects in our study.

3.7 SED Fitting

From Sections 3.1, 3.5, and 3.6, we have the final catalog of all the detected sources from the required images, along with their photometric properties. We know that a star-forming region has many inherent physical properties associated with it, namely Mass, Age, Color, and Size. We therefore find out these properties for each region. To do this, we take the help of Starburst99 [29], which is a spectrophotometric Simple Stellar Population (SSP) model for active star-forming galaxies. This database contains various properties of star clusters such as their Spectral Energy

Distributions, Luminosities, Colors etc. An SED tells us the variation of luminosity of a clump as a function of wavelength. We use these SED's to determine the age of the clump.

Starburst99 has various datasets of SED's for various Initial Mass Functions (IMF's) and various values of metallicities. We download the required datasets for the value of metallicity closest to the one of NGC 4571. We already had the corrected flux values from the analysis of our 7 images belonging to different wavebands. We therefore have 7 values of fluxes for 7 different values of wavelengths. We fit these 7 points to the SED's from the database by use of a custom fitting code which fits the 7 points to each spectrum via CHI^2 minimization fitting. We calculate the residual for each photometric point as follows -

$$\boxed{R = \sum_{i=1}^{7} \left[\frac{(FO_i - FM_i)^2}{FO_i} \right]}$$

Where FO_i is the Observed value of flux in the wavelength in consideration, FM_i is the model value of flux in the wavelength in consideration, and $i \in (FUV, NUV, u, g, r, i, z)$

We have the observed data of the detected clumps for 7 different wavebands. We fit the 35 model spectra of different ages from the Starburst99 database and then find the best fit spectra for each detected clump. The spectra fit with the least value of CHI^2 is determined to be the age of the clump. We also perform extinction of the flux values of this Database according to the Fitzpatrick model [25] with parameters - $E(B-V) = 0.047, R_v = 3.1, A_v = 0.1457$.

Chapter 4

Analysis and Results

4.1 Properties of star-forming clumps

Since our primary aim was to look at the nature of star formation in the detected clumps, we derived some physical properties of the common star-forming clumps detected in FUV and NUV filters. We detected a total of 172 clumps common to the FUV and NUV filters. We use the parameters from SExtractor and photutils to derive the below properties of the clumps.

4.1.1 Size

We estimated the diameter of each star-forming clump listed in the catalog generated from Sections 3.1, 3.3, and 3.5. We used the Ellipse parameter A_IMAGE (in pixels), convert it to degrees, and then to parsecs using the relation below. Here, the Kron radius factor is chosen to be 1.25.

$$Diameter = Semi\ major\ axis \times Kron\ Radius\ factor \times 2 \tag{1}$$

The histogram of Diameter values is shown in Figure 4.1. The bright star-forming clumps identified are found to have a range of diameters between 100 – 1200 pc, with most of them belonging in the range of $\sim 100-400$ pc. We notice that the smaller sized clumps dominate in number, and we also observe a distinct peak at around the ~ 150 pc mark. We also detected 13 sources having diameters greater than 450 pc.

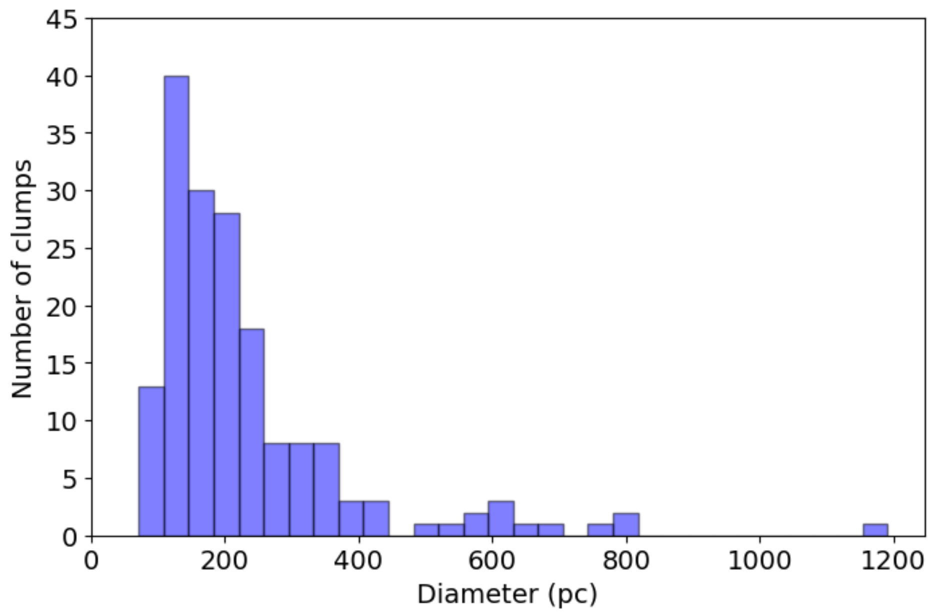

Figure 4.1: Histogram for Sizes of the F154W and N263M matched clumps

4.1.2 Radial Distances

We estimated the Radial distance of each star-forming clump from the center of the galaxy listed in the catalog. We input the galaxy properties (RA and DEC of the center, position angle, distance, and the inclination) and the source properties (RA and DEC of each source) into our custom-defined function, which outputs the Radial distance (in kpc) of the source from the center of the galaxy. We converted the equatorial coordinates to angular coordinates, rotate the coordinate system, de-project the y - coordinate, and then calculate the final angular distance, which is the desired quantity. The workflow is detailed in [5], and the histogram of the Radial distance values is shown in Figure 4.2. The bright star-forming clumps identified are found to have a range of Radial distances between $\sim 0.5-8.5$ kpc, with most of them belonging in the range of $\sim 3-7$ kpc. We also observe a distinct peak at around the ~ 5 kpc mark.

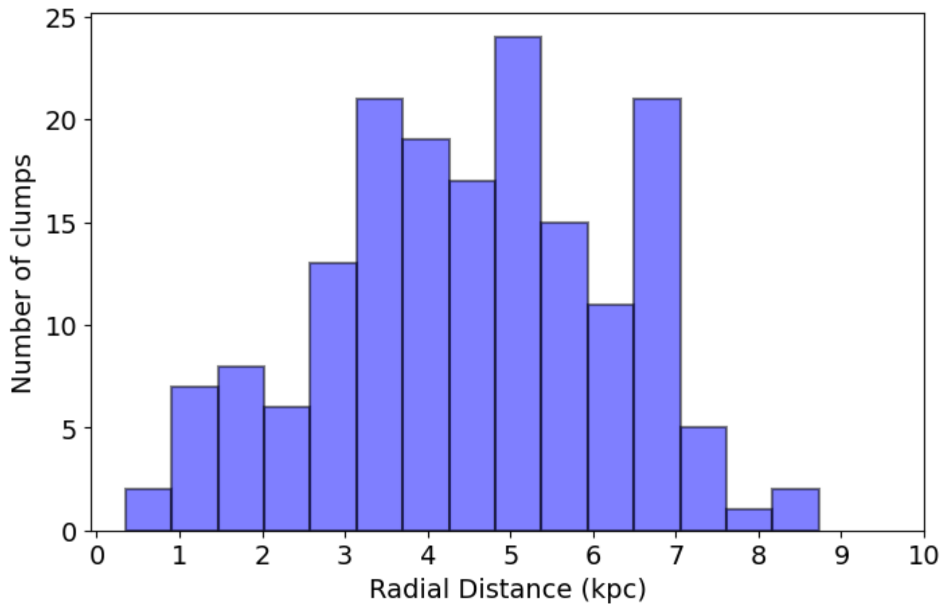

Figure 4.2: Histogram for Radial distances of the F154W and N263M matched clumps

4.1.3 (FUV - NUV) Color

We found out the (FUV - NUV) color of each star-forming clump listed in the catalog by finding out the magnitudes of the sources from their flux values, which were measured in counts per second (CPS). We made sure to account for the Extinction (Section 3.6) and Zeropoint corrections (Section 2.3). The relation used to calculate magnitude values from flux values is shown below -

$$\boxed{mag_{\lambda} = -2.50 \times log_{10}(Flux) + ZP(AB\ magnitude) + A_{\lambda}} \tag{2}$$

We do the procedure for the F154W and the N263M wavelengths and subtract them to find out the (FUV-NUV) color of the clumps, the histogram for which is plotted in Figure 4.3. The bright star-forming clumps identified are found to have a range of color values between $\sim 0.45\ to\ 1.5$, with most of them belonging in the range of $\sim 0.6\ to\ 1.1$. We also observe a distinct peak at around the ~ 0.8 mark. The distribution then tapers off as we go left or right from the peak.

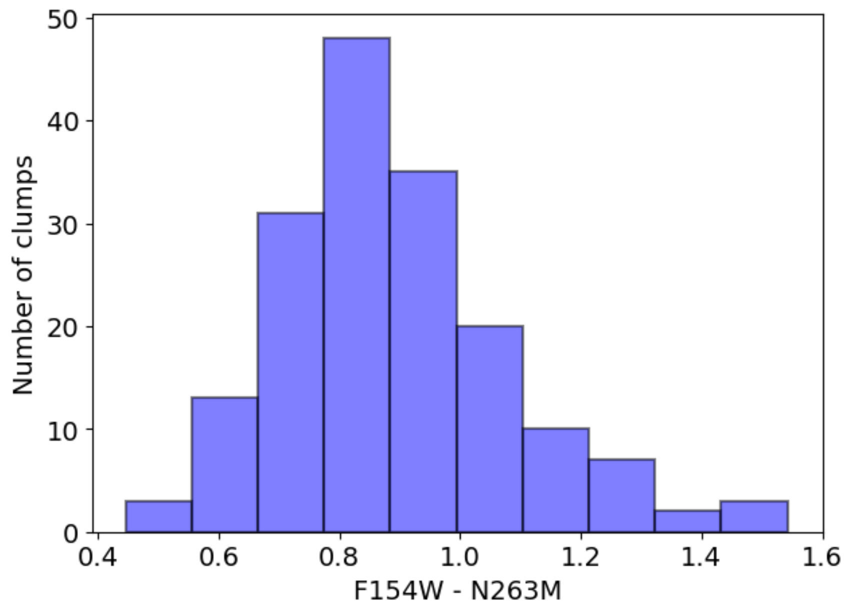

Figure 4.3: Histogram for Color of the F154W and N263M matched clumps

4.1.4 Ellipticity

We estimated the ellipticity of each star-forming clump listed in the catalog. We used the Ellipse parameter ELLIPTICITY $(1-\frac{B}{A})$ from SExtractor and plot its histogram, shown in Figure 4.4. The bright star-forming clumps identified are found to have a range of ellipticity values between $\sim 0.0-0.8$, with most of them belonging in the range of $\sim 0.0-0.5$. We notice that clumps having smaller ellipticity values dominate in number, and we also observe a distinct peak at around the ~ 0.3 mark.

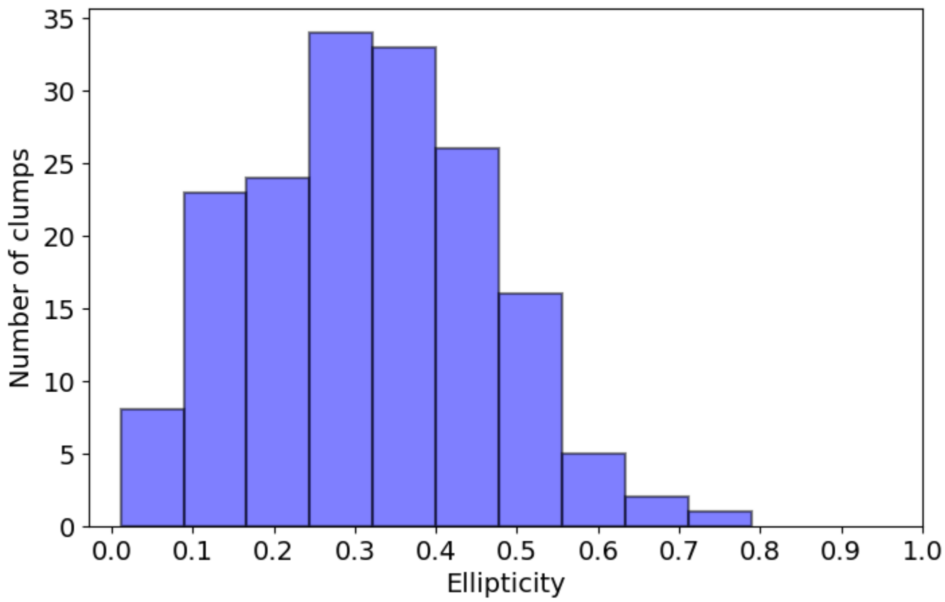

Figure 4.4: Histogram for Ellipticity of the F154W and N263M matched clumps

4.1.5 Position Angles

We estimated the position angle of each star-forming clump listed in the catalog. We used the Ellipse parameter THETA_IMAGE and plot its histogram, shown in Figure 4.5. The bright star-forming clumps identified are found to have a range of position angle values between $\sim(-80\,to\,+80)$, with there being no preferred range for the Position angle values. We also observe a distinct peak at around the $\sim(-20\,to\,0)$ mark.

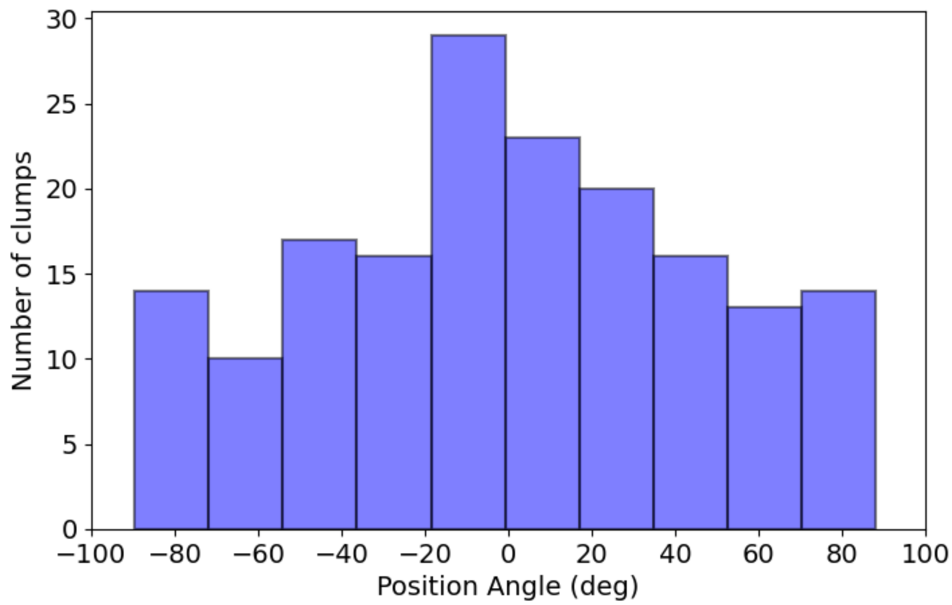

Figure 4.5: Histogram for Position Angles of the F154W and N263M matched clumps

4.1.6 Size vs Radial Distance

We plotted the size and the Radial distances of identified clumps, shown in Figure 4.6. We noticed that clumps closer to the inner part of the galaxy tend to have a larger size as when compared to clumps lying further away in the outside of the galaxy. We also noticed that irrespective of the Radial distance, most of the sources have a size between 100 and 400 pc. A high degree of variation is seen in the sizes of sources in the inner part of the galaxy, this variation decreases as we move away from the galaxy.

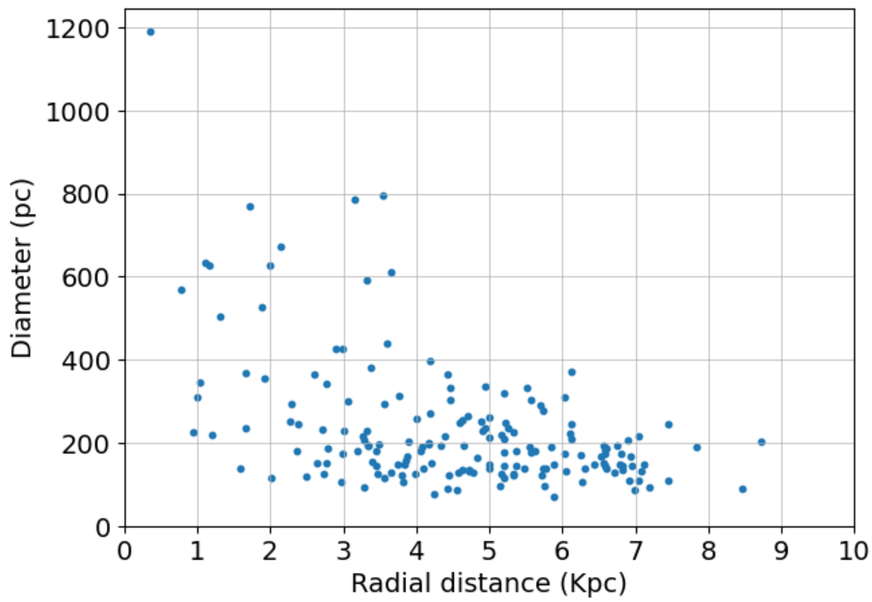

Figure 4.6: Size vs Radial distances of the F154W and N263M matched clumps

4.1.7 Color Magnitude Diagram

We plotted the (F154W - N263M) Color-Magnitude diagram, shown in Figure 4.7. We noticed that sources with a bluer color (more negative value) had smaller F154W magnitudes than the other sources. Most of the sources have a color in the range (~ 0.4 *to* 1.6).

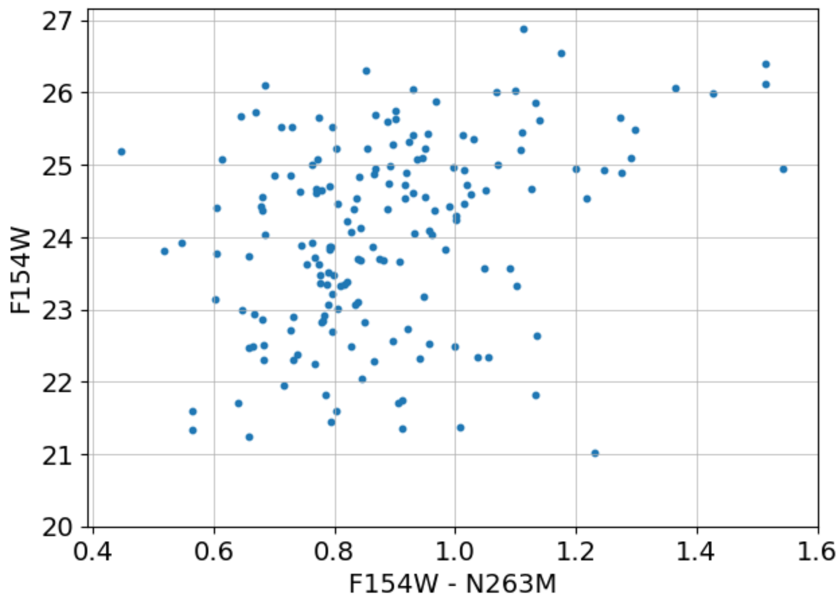

Figure 4.7: CMD of the F154W and N263M matched clumps

4.1.8 Color vs Size

We found out the relation between the Color and the Size of each star-forming clump listed in the catalog. We had estimated the color in Section 4.6 and the Size in Section 4.1 respectively. We therefore plotted them against each other to look at any visible trends. The plot is shown in Figure 4.8. We noticed that the color value of the smaller clumps belong to a range of values between 0.4 & 1.4 and that most of the smaller clumps are bluer in color (negative color value) than the larger clumps. We also note that the largest clumps detected are bluer than some of the smallest clumps detected. We had also noticed a wide variation in the color values in smaller clumps, this variation decreases as the size of the clumps increase. Most of the clumps lie within the range $\sim 100\ to\ 400$ pc for size and $\sim 0.6\ to\ 1.2$ for color

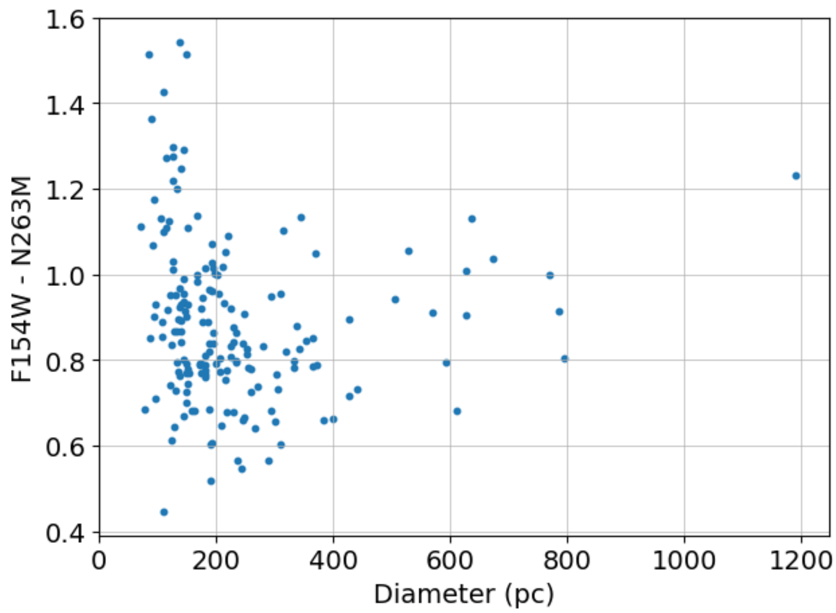

Figure 4.8: Color vs Size of the F154W and N263M matched clumps

4.1.9 Color vs Radial Distance

We found out the relation between the Color and the Radial Distance of each star-forming clump listed in the catalog. We had estimated the color in Section 4.6 and the Radial distance in Section 4.2 respectively. We therefore plotted them against each other to look at any visible trends. The plot is shown in Figure 4.9. We noticed that the color of the clumps gets bluer as we move to the outer parts of the galaxy, and this is very well seen in the middle regions of the galaxy. There are however, a few sources present in the outskirts of the galaxy, which are redder than almost all sources lying further inside the galaxy.

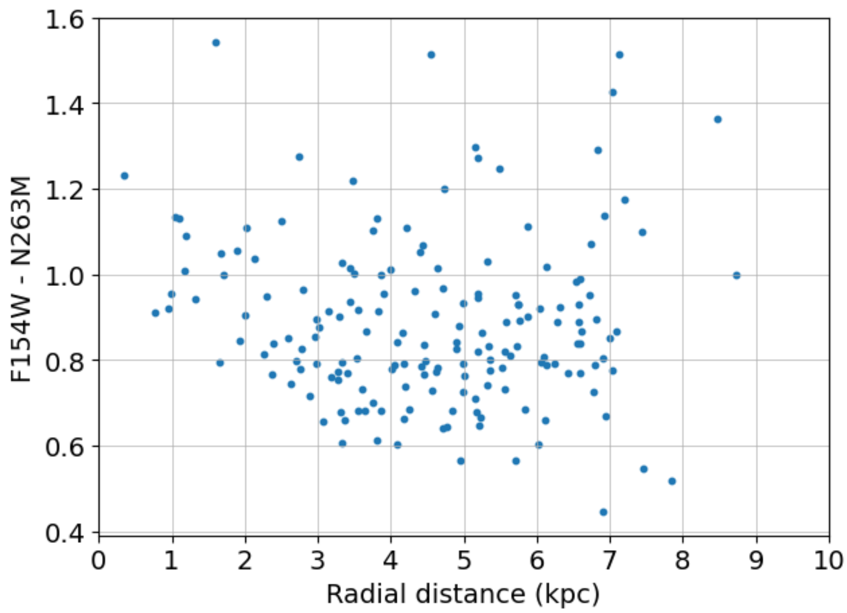

Figure 4.9: Color vs Radial distances of the F154W and N263M matched clumps

4.1.10 SFR of individual clumps

The SFR density for a clump is an estimate of the rate of Star formation in the clump. We used the scaling relation given in Eq 2 in [6] to estimate the SFR. Here, mag_{FUV} is the area normalized and extinction corrected FUV magnitude, and D is the distance to the galaxy in Mpc. We found out the SFR density of each star-forming clump listed in the catalog by using the scaling relation below -

$$\boxed{log(SFR_{FUV}(M_{\odot}/yr/kpc^2)) = 2.78 - (0.4 \times mag_{FUV}) + 2\ log(D)} \tag{3}$$

The Histogram of SFR density values is plotted in Figure 4.10. The SFR density values of the FUV and NUV bright clumps identified in NGC 4571 are found to have a range of values between $(0.001 - 0.008)$ $M_{odot}/yr/kpc^2$, with most of them belonging in the range of $\sim$ $(0.001 - 0.003)$ $M_{odot}/yr/kpc^2$. We notice that clumps having smaller SFR density values are more in number, and we also observe a distinct peak at around the ~ 0.001 mark.

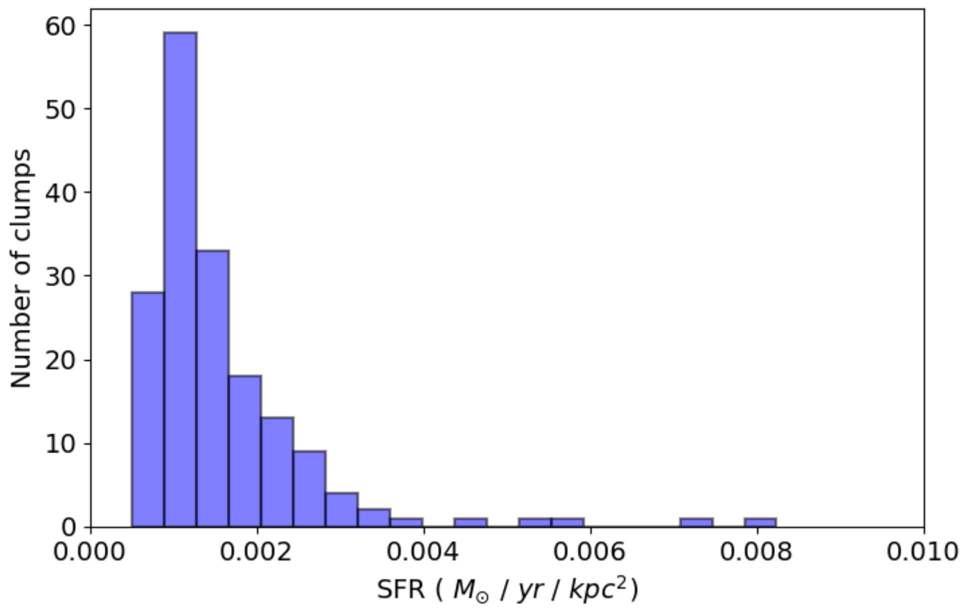

Figure 4.10: Histogram for SFR Density values of the F154W and N263M matched clumps

4.2 Determination of Age

We estimated the age of each star-forming clump listed in the catalog. In order to characterize the star-forming regions in NGC 4571, we will use the Starburst99 SSP model. We carry out the steps detailed in Section 3.7, obtain the least CHI^2 values, and thereafter, the age of each clump. We plot all the obtained ages individually as the ages of the SED's in Starburst99 are discrete and finite in number. We plot the Age histogram of the detected clumps in Figure 4.11. We see the ages take up a range of values, with most of the clumps having their ages between 1 and 20 Myr, whilst the ages of the other clumps belong to a range of values between 30 and 900 Myr. We also see intermittent peaks of almost similar number, albeit in irregular intervals.

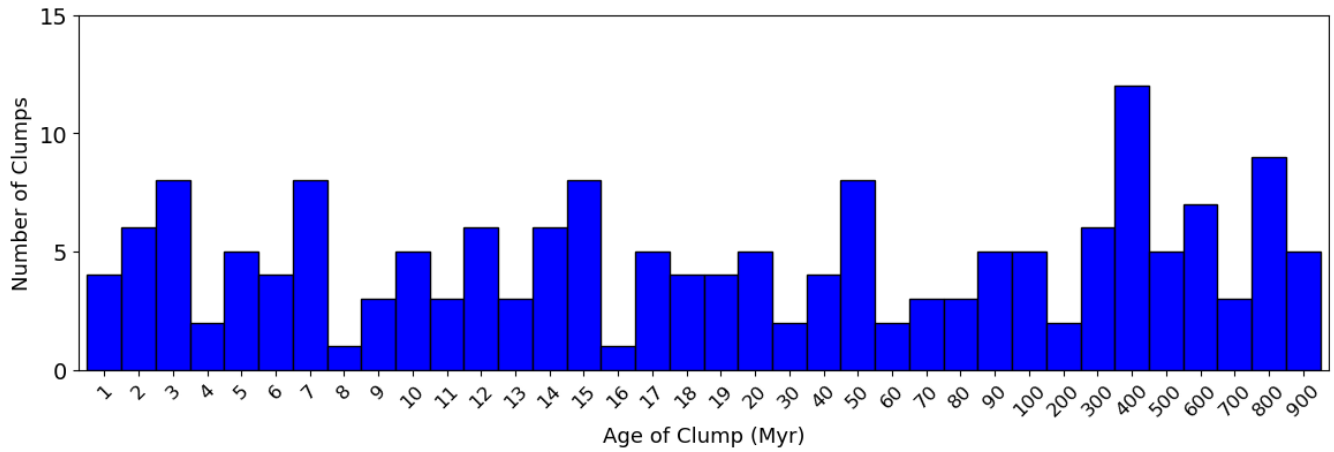

Figure 4.11: Age Histogram of the F154W and N263M matched clumps

4.3 Distribution of Age

The Spatial distribution of star-forming clumps as a function of age gives us insight into the history of star formation in the galaxy. This map also gives us crucial information about the natural environment of the galaxy, and whether there were mechanisms and events which could have had triggered star formation across the galaxy. This also helps us to study the nature of the disk growth in the galaxy. To visualize the spatial distribution of the identified star-forming clumps, we divide them into 4 different age groups between 1 and 900 Myr. The age range of the groups are 1-10 Myr, 10-20 Myr, 20-200 Myr, 200-900 Myr. The age range is chosen by looking at Figure 4.10. We fixed the interval to be smaller where there were more number of clumps seen, and the interval size was chosen to be larger where there were a smaller number of clumps observed. The number of sources in each age group are 46, 45, 34, and 47 respectively. The locations are shown in Figures 4.12 and 4.13.

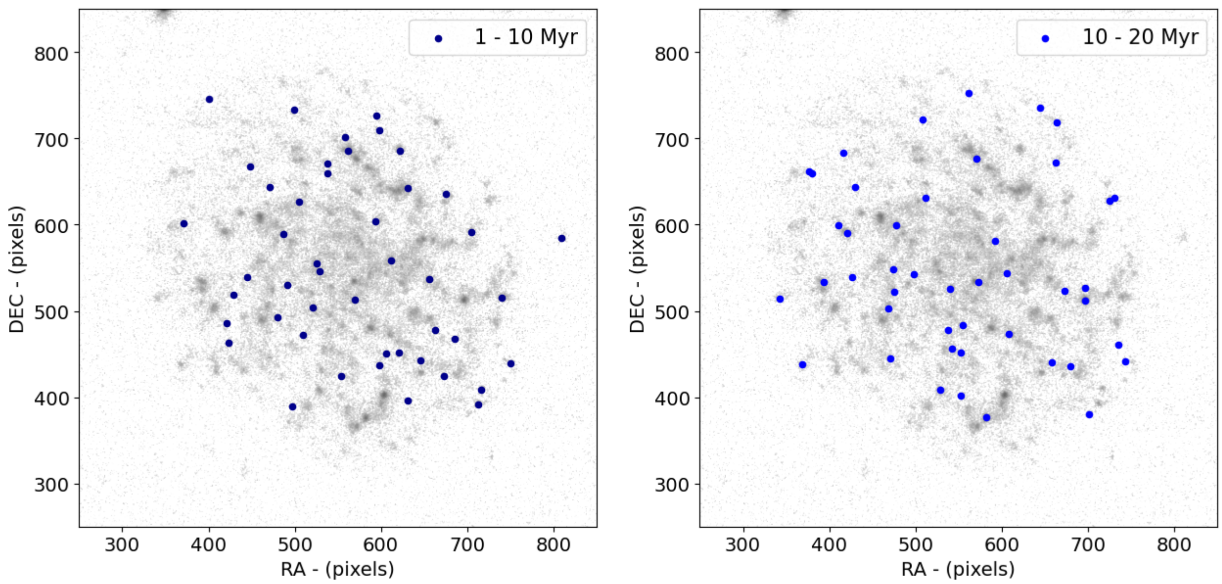

Figure 4.12: Spatial Age distribution for sources aged 1-10 Myr (left) and 10-20 Myr (right)

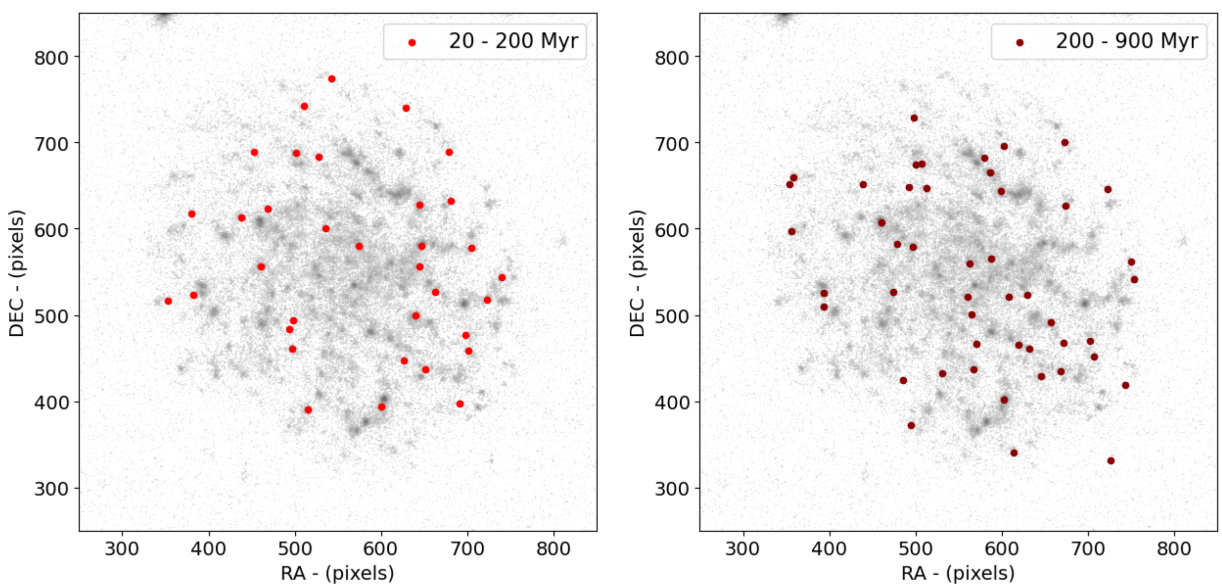

Figure 4.13: Spatial Age distribution for sources aged 20-200 Myr (left) and 200-900 Myr (right)

We notice that most of the clumps located in the outermost extent of the galaxy are younger in age, although there are younger clumps present in the interior of the galaxy too. The number of clumps present in the 1-10 Myr and 10-20 Myr are similar in number, and these 2 age groups combine to contribute $\sim 53\%$ of the total number of detected clumps. The 20-200 Myr group contains the least number of clumps. The clumps in the innermost parts of the galaxy are found to belong to the younger age group (1-10 and 10-20 Myr), as well as the older group (200-900 Myr). The distributions of clumps is found to be all around the galaxy, regardless of the age of the clump. The consensus here is that there has been a galaxy-wide process of star formation occurring during the last 20 Myr of the galaxy's lifetime.

4.4 Radial Surface Brightness Profile

The Radial Surface Brightness profile of the galaxy gives us critical information regarding the distribution of the star-forming regions in the galaxy. Since NGC 4571 has been imaged in 2 UV wavebands (1 FUV and 1 NUV), we constructed the SBP for both of those filters. We also constructed the SBP of the SDSS optical filters (g and r). Assuming the values of the inclination and Position angles of the galaxy, we found out the Radial distance of all clumps from the centre of the galaxy, as detailed in Section 4.2. Taking the values of the Right Ascension (RA), Declination (DEC), and Position Angle (PA) of the galaxy from table 1.1, we created concentric elliptical apertures, each of width $\sim 0.43\ kpc$. We then measured the area of each annulus (area between two consecutive ellipses), along with the total CPS flux in each of them. We then corrected the CPS flux for background and extinction and also multiplied with the corresponding Unit Conversion factors. We then defined the distance of the apertures from the center of the galaxy to be the Radial Distance from the center of the galaxy. We then define the flux density to be the normalization of the flux values in that annulus with the area of that particular annulus in consideration. We then plotted this quantity with respect to the Radial distance from the galaxy. The Radial Surface Brightness Profile for the galaxy in the FUV and NUV bands as a function of Radial distance is shown in Figure 4.14, and the corresponding profile for the optical g and r bands is shown in Figure 4.15.

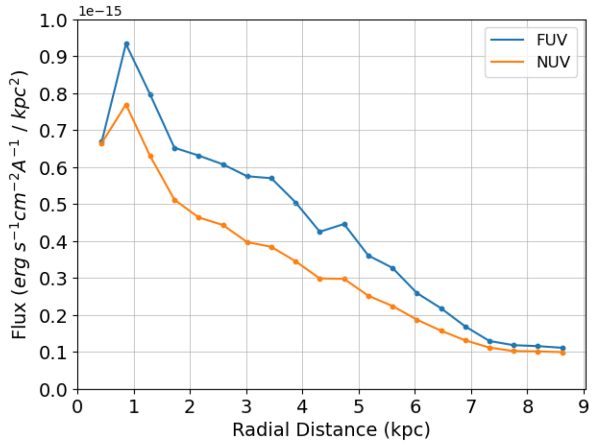

Figure 4.14: Radial Flux density profile for FUV and NUV bands

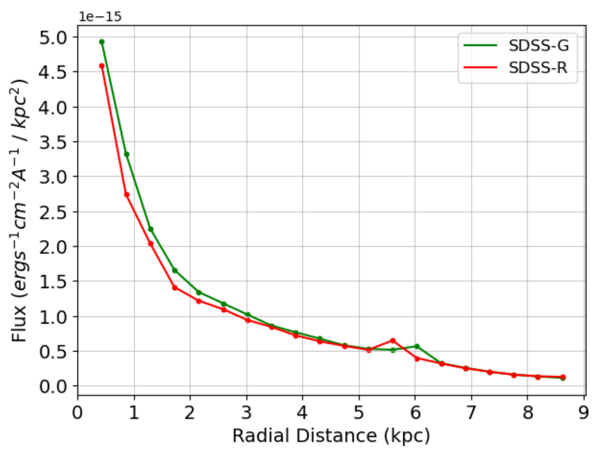

Figure 4.15: Radial flux density profile for optical r and g bands

The Surface Brightness profile of UVIT shows a dip in the central region of the galaxy. It then peaks at $\sim 1.0\ kpc$, which points towards an increased star formation activity in the central region of NGC 4571. Beyond 1.0 kpc, the value decreases all the way to the edge of the galaxy till $\sim 9.0\ kpc$ apart from a very slight increase between $\sim 4.2\ kpc$ & 4.7 kpc.

We know that the FUV and NUV bands trace the stellar populations at ages around $\sim 100\ Myr$ and $\sim 200\ Myr$ respectively. Therefore an increase in flux would imply an increase in the number of such sources. Although we do not get any information about the ages of these sources, we have enough information to determine the type of sources detected. The increase in Surface Brightness between $\sim 0.5\ kpc$ & $1.0\ kpc$ corresponds to the presence of FUV and NUV bright regions emitting FUV and NUV radiation, therefore indicating the presence of comparatively younger sources in this region.

4.5 Radial Color Profile

The radial color profile helps us investigate the relative flux variation between the FUV and NUV wavebands. We calculated the color value for each aperture from the magnitude value, which itself is calculated from relation (2), and plotted it with respect to the radial distance from the galaxy, shown in Figure 4.16.We also calculated and plotted the photometric error in the form of error bars. We noticed a decrease in the color value right from $0.0\ kpc$ to $\approx\ 3.5\ kpc$, which signifies the color becoming bluer with an increase in radius. Beyond $3.5\ kpc$, there is a stage of fluctuation to $\approx\ 5.5\ kpc$. The trend then reverses as we see an increase in the color value, implying that the color becomes redder with Radial distance. There is a continuous increase up till $\sim 9\ kpc$, where we see the increase slowing down from $\approx 7.2\ to\ 9.0\ kpc$.

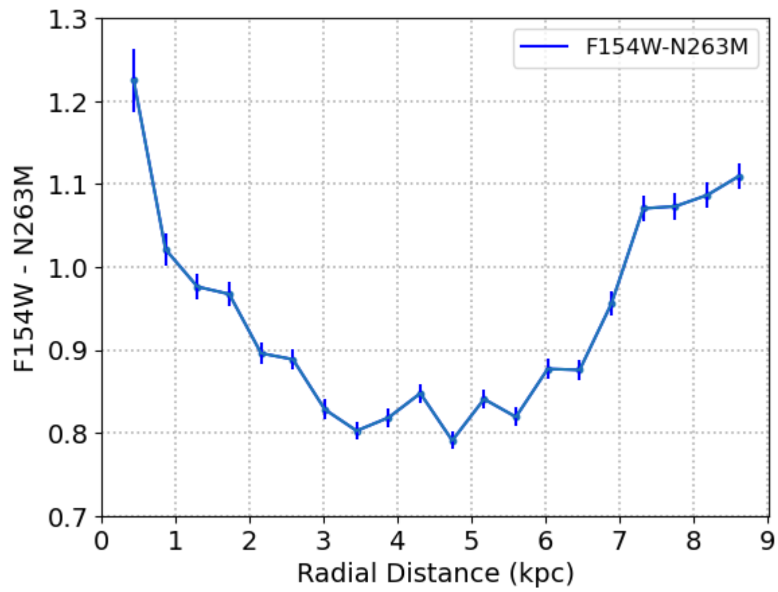

Figure 4.16: Radial (FUV-NUV) Color profile of the galaxy

This plot is a good diagnostic for the types of sources present in the galaxy. The color value decreases relatively steeply at first, indicating the presence of ”bluer” (younger) sources in that particular annulus. The decrease then becomes slow and gradual until ~ 3.5 *kpc*, where we see intermittent increments and decrements in the color value. In a way, the decrease in color value between 0.5 *kpc* & 1.0 *kpc* is in agreement with the increase in surface brightness. The presence of bluer sources in a particular region of the galaxy indicates the presence of favorable conditions for star formation.

4.6 Radial SFR Density Profile

The Radial star formation Rate (SFR) density profile of a galaxy gives us information concerning the SFR of the galaxy in concern. Looking at the radial SFR profile will give us a good idea of the locations where star formation is seen the most, which would help us explain the origins of the process. In order to estimate the radial SFR profile of the galaxy, we used the F154W band (FUV) image of the galaxy. We used the same apertures used in Section 4.12 and normalized the flux values for all of those apertures with respect to their respective areas. We then converted the flux values to the corresponding magnitude values and corrected to account for the extinction using the relation (3). The Radial SFR Density Profile is shown in Figure 4.17. We also00 calculated and plotted the photometric error in the form of error bars. The SFR density is found to increase from the central region of the galaxy all the way upto ~ 1.0 *kpc*, which suggests that SFR density is dominated by regions located within a radius of 1.0 *kpc*. Beyond 1.0 *kpc*, the SFR density starts to decrease, drastically until ~ 2.0 *kpc*, and steadily thereafter until 10 *kpc* There is a region between 4.2 *kpc* & 4.8 *kpc*, where we observed a slight increase in SFR density.

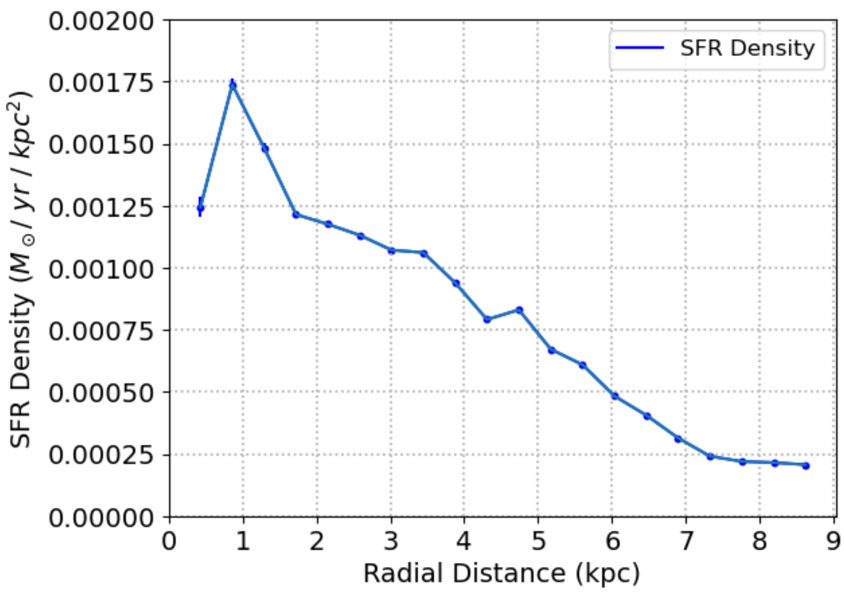

Figure 4.17: Radial SFR Density profile of the galaxy

4.7 Correlation between Age and Distance of sources

We overlayed the detected sources on the FUV image and color-coded them according to the age group to which they belong. We also overlayed the previously-used apertures (of width 0.43 pc) which were defined in Section 4.4. The final diagram, complete with the overlaying is shown in

Figure 4.18.

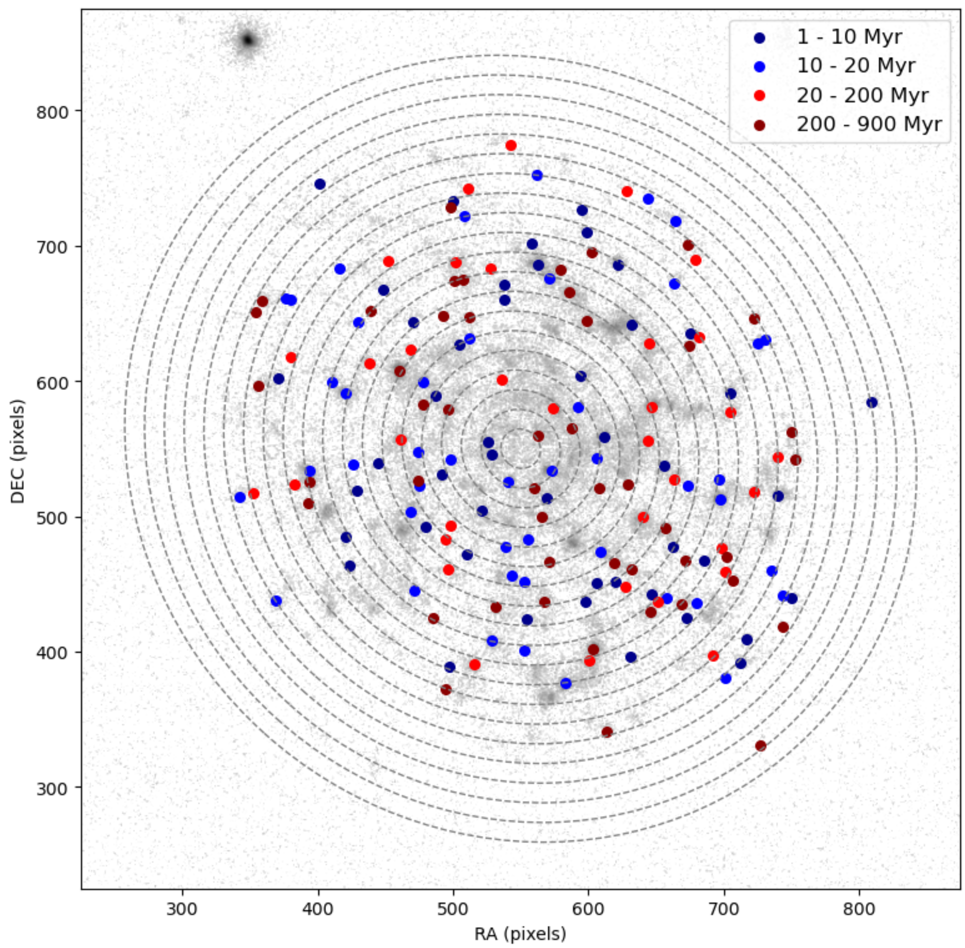

Figure 4.18: Apertures overlayed along with Detected and Age-categorized sources

The bright young star-forming clumps identified are located all over the galaxy, with no apparent particular distribution of sources with regards to age or location. We noted that the youngest sources coded in dark blue and blue are seen all over the galaxy. The Age-distance distribution of sources correlate well with the Surface Brightness Profile derived in Section 4.4. The spike in the second aperture at ~ 1.0 *kpc* observed in Figure 4.14 correlates very well with the observation from the figure that the central region of the galaxy is being populated with young sources of the younger age groups.

Chapter 5

Discussion

The primary objective of this thesis was to study the galaxy NGC 4571 and identify the young star-forming clumps located throughout the galaxy. To accomplish that, we used the FUV and NUV images of the galaxy, which was observed in the F154W and N263M filters of UVIT. The superior spatial resolution of the UVIT $\sim 1.4''$ enabled us to identify clumps of diameter upto ~ 800 *pc*. We measured the fluxes of the identified star-forming regions and compared them with the model fluxes in order to estimate the age of the clumps.

We used the SED data from the Starburst99 SSP model, which helped us to estimate the ages of the clumps. Therefore, errors in the SED data could be reflected on our estimates of the ages of the clumps. Another significant parameter which could affect our age estimate is the extinction parameter. We have assumed a fixed value of the reddening in the galaxy, which is almost never the case as the spatial variation in the values isn't accounted for. This in turn would affect the value of the observed flux of the star forming clumps. A larger value of the reddening parameter would make the clumps younger than usual and vice versa. Another parameter worth noticing is the metallicity of the galaxy. We couldn't find any reliable estimates of the metallicity, and thus were forced to use the value of solar metallicity. The identified clumps might also have their own values of metallicity, which could further affect other parameters as for a fixed value of age, the value of the color changes with metallicity.

This galaxy hasn't been studied in great detail, especially the star forming capabilities of the galaxy. Our work however presents evidence of ongoing star formation. The UVIT surface brightness profile of the galaxy shows a peak near the center of the galaxy, which is an indicator of the presence of star-forming regions. We also noticed that the FUV profile takes over the NUV profile and stays the same way up till our observed value of radial distance $\sim 9\ kpc$. The FUV and NUV profiles also become flatter in the region between 7 and 9 kpc, which corresponds to the outer regions of the galaxy. The difference between the FUV and NUV flux is the most in the region between 2 and 6 kpc, it is in this region where the identified clumps are found to be mostly bluer in color. This signifies that the clumps found in this region are mostly younger in age. There is a drastic drop in the FUV and NUV fluxes beyond 5 kpc, which is an indicator of a decreased presence of younger and massive sources. This is reflected in the radial color profile, whern it is seen that the value of the color increases from the 5 kpc mark all the way upto the outer extents of the galaxy.

The SDSS surface brightness profile shows a continuous and a rather drastic decreasing trend, apart from a slight bump in the brightness at around the 6 kpc mark. This decreasing trend is typical of optical emission as the central bulge of the galaxy is the biggest contributor to the brightness of a galaxy in the optical wavelengths. The g and r profiles almost mirror each other in their trends, the g profile tends to lead the r profile throughout the increasing radial distance.

In our study, we also found out that $\sim 53\%$ of the identified FUV and NUV clumps are younger than 20 Myr, which is an indicator of a recent episode of star formation in the galaxy during the last 20 Myr. Our study also found out that the younger clumps are distributed throughout the galaxy, which points towards a galaxy-wide episode of star formation. Our study also shows that the central region has no star formation as looking at the FUV and NUV images, we can see the sources located in a ring-like structure around the central region of the galaxy.

The SFR density profile of the galaxy shows a good correspondence with the radial color profile. The peak observed near the central region in the SFR profile corresponds with the decrease in the color value from 1.2 to 1.0, indicating the presence of young star-forming regions in that particular region. The decrease in the color value is visible right through upto the 4 kpc mark. The SFR density starts to decrease from this point onwards, and keeps on decreasing until the outer extents of the galaxy (~ 8.5 pc). The corresponding change is also seen in the color profile, as the color value starts to increase from around 0.8 at the 7 kpc mark and reached a value of 1.1 at around 9 kpc. This is an indicator of the lack of younger and bluer sources present in that region. The flattening of the SFR density profile from 7 to 9 pc also corresponds well with the initial increase and corresponding flattening of the color profile in the exact same region. This flattening also corresponds with the absence of young star forming regions in the outermost extents of the galaxy.

Chapter 6

Conclusions

The main results from our study are summarized below -

1. We used UVIT FUV and NUV observations to identify the star-forming clumps in the galaxy NGC 4571, and to understand the UV disk emission profile.

2. We compared the UVIT data with the optical SDSS data. The UV emission shows that there is widespread Star-formation throughout the galaxy. The optical data doesn't show much emission, especially in the outer parts of the galaxy.

3. We identified 172 young star-forming clumps common in the FUV and NUV filters in the galaxy with their sizes ranging between $\approx 100-400$ pc.

4. We measured the FUV and NUV fluxes, sizes, Radial distances, and (FUV-NUV) color values of these clumps.

5. We noticed both the FUV and NUV emission to be spread out throughout the galaxy and extending upto its outskirts.

6. We traced the color of the clump with its Size. We noticed that an increase in the size corresponded with the color getting redder.

7. We traced the color of the clump with its Radial distance from the center of the galaxy. We found that the star-forming clumps are redder in the inner regions of the galaxy, and that the color of the source gets bluer with increasing radii for a majority of the sources. There is however a small yet significant number of sources present, the color for which gets redder with increasing radii. This suggests that the star-formation is more intense in the middle and the outer part of the galaxy as compared with the outskirts of the galaxy.

8. The majority of the star-forming clumps $\sim 53\%$ were found to have an age younger than 20 Myr. This signifies a recent enhancement in the star-formation activity throughout the galaxy.

9. The youngest sources of ages younger than 10 Myr were also found to be spread out all across the galaxy.

10. There are a significant number of sources present in the Age group 200-900 Myr.

11. The UV emission is found to be present up to a Radial distance of ≈ 9 kpc, with most of the flux originating within a radius of ≈ 1 kpc.

12. The SFR of the galaxy is found to be 0.01605 $M_{\odot}/yr$

Bibliography

[1] Arnouts S Bertin E. *SExtractor: Software for source extraction*. 1996.

[2] Luciana Bianchi. Galex and star formation. *Astrophysics and Space Science*, 2011.

[3] A Bosma. 21-cm line studies of spiral galaxies. ii. the distribution and kinematics of neutral hydrogen in spiral galaxies of various morphological types. *Astronomical Journal*, 1981.

[4] Jason A. et al Cardelli. The relationship between infrared, optical, and ultraviolet extinction. *The Astrophysical Journal*, 1989.

[5] M R L Cioni. The metallicity gradient as a tracer of history and structure: the magellanic clouds and m33 galaxies. *Astronomy and Astrophysics*, 2009.

[6] M R L Cioni. Star formation properties in the local volume galaxies via h-alpha and far-ultraviolet fluxes. *The Astronomical Journal*, 2013.

[7] A. Adamo. et al. Probing the role of the galactic environment in the formation of stellar clusters, using m83 as a test bench. *Monthly Notices of the Royal Astronomical Society*, 2015.

[8] Aaron A Dutton et al. A revised model for the formation of disk galaxies: Low spin and dark halo expansion. *The Astrophysical Journal*, 2007.

[9] Bela Abolfathi et al. The fourteenth data release of the sloan digital sky survey. *The Astrophysical Journal Supplement Series*, 2017.

[10] C Giovanardi et al. Effects of environment on neutral hydrogen distribution for disk galaxies in the virgo cluster area. *The Astrophysical Journal*, 1983.

[11] Calzetti D et al. Legacy extragalactic uv survey (legus) with the hubble space telescope. i. survey description. *The Astronomical Journal*, 2015.

[12] Dan Coe et al. Clash: Three strongly lensed images of a candidate z = 11 galaxy. *The Astrophysical Journal*, 2013.

[13] David A Thilker et al. A search for extended ultraviolet disk (xuv-disk) galaxies in the local universe. *The Astrophysical Journal Supplement Series*, 2007.

[14] David Carter et al. The spatial distribution and origin of the fuv excess in early-type galaxies. *Monthly Notices of the Royal Astronomical Society*, 2011.

[15] Hwang H.S. et al. Activity in galactic nuclei of cluster and field galaxies in the local universe. *Astronomy and Astrophysics*, 2012.

[16] Janice C Lee et al. Comparison of h-alpha and uv star formation rates in the local volume: Systematic discrepancies for dwarf galaxies. *The Astrophysical Journal*, 2009.

[17] Kevin Schawinski et al. The green valley is a red herring: Galaxy zoo reveals two evolutionary pathways towards quenching of star formation in early- and late-type galaxies. *Monthly Notices of the Royal Astronomical Society*, 2014.

[18] Mamuru Doi et al. Photometric response functions of the sdss imagers. *The Astronomical Journal*, 2010.

[19] Mark Danovich et al. Four phases of angular-momentum buildup in high-z galaxies: from cosmic-web streams through an extended ring to disc and bulge. *Monthly Notices of the Royal Astronomical Society*, 2015.

[20] N. Bastian. et al. Stellar clusters in m83: formation, evolution, disruption and the influence of the environment. *Monthly Notices of the Royal Astronomical Society*, 2012.

[21] Rahul Shetty. et al. Global modeling of spur formation in spiral galaxies. *The Astrophysical Journal*, 2006.

[22] Robert C. Kennicutt et al. Star formation in the milky way and nearby galaxies. *Annual Review of Astronomy and Astrophysics*, 2012.

[23] S N Tandon et al. In-orbit calibrations of the ultraviolet imaging telescope. *The Astronomical Journal*, 2017.

[24] Searle Leonard et al. The history of star formation and the colors of late-type galaxies. *The Astrophysical Journal*, 1973.

[25] Edward L. Fitzpatrick. Correcting for the effects of interstellar extinction. *The Publications of the Astronomical Society of the Pacific*, 1999.

[26] R C Kennicutt Jr. Effects of environment on neutral hydrogen distribution for disk. *Astronomical Journal*, 1983.

[27] Robert C. Kennicutt Jr. Star formation in galaxies along the hubble sequence. *Annual Review of Astronomy and Astrophysics*, 1998.

[28] Amit. et al Kumar. Ultra violet imaging telescope (uvit) on astrosat. *Space Telescopes and Instrumentation 2012: Ultraviolet to Gamma Ray*, 2012.

[29] Claus. et al Leitherer. Starburst99: Synthesis models for galaxies with active star formation. *The Astrophysical Journal Supplement Series*, 1999.

[30] Christopher D Martin. The galaxy evolution explorer: A space ultraviolet survey mission. *The Astrophysical Journal*, 2005.

[31] Smithsonian Astrophysical Observatory. Saoimage ds9: A utility for displaying astronomical images in the x11 window environment. *Astrophysics Source Code Library*, 2000.

[32] M.B. Taylor. Topcat & stil: Starlink table/votable processing software. *Astronomical Data Analysis Software and Systems XIV ASP Conference Series*, 2005.

[33] B. M. Tinsley. Galactic evolution: Program and initial results. *Astronomy and Astrophysics*, 1972.

[34] S van den Bergh. A new classification system for galaxies. *Astrophysical Journal*, 1976.